



**AFRL-OSR-VA-TR-2013-0438**

---

**Carbohydrate Nanotechnology: Hierarchical Assemblies and Information Processing with Oligosaccharide-Synthetic Lectin Host-Guest Systems**

**Prof. Adam B. Braunschweig**

New York University  
70 Washington Square S  
New York, NY 10012-1019

---

**08/05/2013**

**Final Report**

**DISTRIBUTION A: Distribution approved for public release.**

Air Force Research Laboratory  
AF Office Of Scientific Research (AFOSR)/RTB1

**REPORT DOCUMENTATION PAGE**
*Form Approved  
OMB No. 0704-0188*

The public reporting burden for this collection of information is estimated to average 1 hour per response, including the time for reviewing instructions, searching existing data sources, gathering and maintaining the data needed, and completing and reviewing the collection of information. Send comments regarding this burden estimate or any other aspect of this collection of information, including suggestions for reducing the burden, to Department of Defense, Washington Headquarters Services, Directorate for Information Operations and Reports (0704-0188), 1215 Jefferson Davis Highway, Suite 1204, Arlington, VA 22202-4302. Respondents should be aware that notwithstanding any other provision of law, no person shall be subject to any penalty for failing to comply with a collection of information if it does not display a currently valid OMB control number.

**PLEASE DO NOT RETURN YOUR FORM TO THE ABOVE ADDRESS.**

1. REPORT DATE (DD-MM-YYYY) 08/05/2013	2. REPORT TYPE Final Technical	3. DATES COVERED (From - To) 04/01/2011 to 02/28/2013		
4. TITLE AND SUBTITLE  Carbohydrate Nanotechnology: Hierarchical Assemblies and Information Processing with Oligosaccharide-Synthetic Lectin Host-Guest Systems		5a. CONTRACT NUMBER		
		5b. GRANT NUMBER FA9550-11-1-0032		
		5c. PROGRAM ELEMENT NUMBER		
6. AUTHOR(S) Prof. Adam B. Braunschweig		5d. PROJECT NUMBER		
		5e. TASK NUMBER		
		5f. WORK UNIT NUMBER		
7. PERFORMING ORGANIZATION NAME(S) AND ADDRESS(ES) New York University 70 Washington Square S New York, NY 10012-1019		8. PERFORMING ORGANIZATION REPORT NUMBER		
9. SPONSORING/MONITORING AGENCY NAME(S) AND ADDRESS(ES) AFOSR 875 N. Randolph St Arlington, VA 22203		10. SPONSOR/MONITOR'S ACRONYM(S)		
		11. SPONSOR/MONITOR'S REPORT NUMBER(S)		
12. DISTRIBUTION/AVAILABILITY STATEMENT Choose one: A = Approved for public release; distribution is unlimited				
13. SUPPLEMENTARY NOTES				
14. ABSTRACT  Carbohydrates are used throughout nature to direct information processing and hierarchical assembly, but are rarely explored in the context of synthetic nanotechnology. Carbohydrates were explored as targets for synthetic receptors, in nanopatterning, and for directing the movement of nanoswimmers. A synthetic carbohydrate receptor that achieves the highest reported selectivity for mannoses over other pyranosides (28:1) via a unique cooperative binding mechanism has been developed. At high temperatures, a 2:1 receptor : mannose complex forms, and at low temperatures, a 1:2 receptor : mannose complex forms. The structures and thermodynamic binding properties of these complexes have been characterized by nuclear magnetic resonance spectroscopy and molecular modeling. Additionally, Polymer Pen Lithography has been combined with the copper catalyzed azide-alkyne click reaction and the Staudinger Ligation, two bioorthogonal organic reactions, to create functional carbohydrate arrays. This patterning approach controls the position, orientation, and feature diameter of the deposited molecules to create sub-1 micrometer features of carbohydrates across centimeter-scale areas. Finally, a new mathematical model that describes the flipping, turning, and dispersion of gold-platinum catalytic nanomotors has been derived that explains their diffusion over long times and accounts for the imperfections on the nanorod structures that inevitably arise during any manufacturing process.				
15. SUBJECT TERMS				
16. SECURITY CLASSIFICATION OF: a. REPORT unclassified		17. LIMITATION OF ABSTRACT unclassified (U)	18. NUMBER OF PAGES	19a. NAME OF RESPONSIBLE PERSON Adam B. Braunschweig
b. ABSTRACT unclassified				19b. TELEPHONE NUMBER (Include area code) (305) 284-2516
DISTRIBUTION A: Distribution approved for public release				

**AFOSR Final Report**

**Carbohydrate Nanotechnology: Hierarchical Assemblies and Information Processing  
with Oligosaccharide-Synthetic Lectin Host-Guest Systems**

**Grant Number: FA9550-11-1-0032**

**Principal Investigator:**  
**Adam B. Braunschweig**  
**a.braunschweig@miami.edu**  
**Phone: (305) 284-2516**

**Department of Chemistry**  
**New York University**  
**100 Washington Square East**  
**New York, NY 10003**

**July 2013**

**Period covered by this report:**

**4/1/11 to 2/28/13**

## A. Introduction and Objectives

Self-assembly provides an attractive route from simple building blocks to hierarchical nanomaterials whose sophistication and function rival those found in living systems. Nature uses the cooperative and multivalent interactions between carbohydrates and the proteins that bind them, termed lectins, to direct the formation of larger aggregates, such as tissues, organs, and ultimately organisms. Despite their increased information density relative to other recognition elements (DNA base pairs, peptides, etc.) currently used to assemble hierarchical nanosystems (Table 1), carbohydrates have not been adopted by researchers because natural lectins are too complex to use in the context of synthetic nanotechnology, and the intricacies of oligosaccharide structure makes designing specific hosts that can discriminate between different monosaccharides particularly difficult. While there is significant interest in developing synthetic lectins, this task remains challenging because monosaccharides contain several hydroxyl functions and multiple stereocenters per residue, and they typically occur as a constantly fluctuating mixture of 5- and 6-membered rings. However, the multivalency and cooperativity inherent to saccharide binding could add significant capabilities to synthetic nanotechnology. Both carbohydrates and lectins typically exist as multimeric assemblies, and the high affinity that arises from multivalent interactions leads to the error-correcting that is characteristic of biological self-assembly. Moreover, binding in lectins can change as a function of the cooperativity that arises from the interplay of two or more interactions with the same receptor, so that the system as a whole behaves differently than the mere multiplication of individual interactions would predict. *The goal of the research program was to utilize oligosaccharide-synthetic lectin binding pairs to direct the assembly of self-organized, hierarchical materials and to employ the binding properties of these structures to create synthetic nanosystems for information storage and processing.* To that end, three synergistic objectives were pursued: (1) develop saccharide- synthetic lectin binding pairs that bind specifically and strongly through noncovalent interactions, (2) utilize the information encoded by the oligosaccharide structure to design advanced hierarchical materials for molecular logic operations, (3) employ cooperative and multivalent binding interactions between carbohydrates and synthetic lectins to drive mesoscopic assembly in solution, in polymers, and on surfaces. The major questions asked were: How can synthetic lectins that discriminate between monosaccharides that differ by only the orientation of a single hydroxyl be developed? How can the conformational and binding dynamics inherent to saccharides be used in molecular logic? Can synthetic lectins employ multivalency and cooperativity to control the structure and dynamics of nanomaterials in three dimensions?

**Table 1. Carbohydrate Information Density.** The information density of biopolymers can be considered the number of different molecules ( $N$ ) that can be made from an oligomer of a given size ( $S$ ). For nucleotides,  $N = 4^S$  and for peptides  $N = 20^S$ , but for carbohydrates the equation is far more complex.

Number of Different Oligomers			
Oligomer Size	Nucleotides	Peptides	Carbohydrates
1	4	20	20
2	16	400	1,360
3	64	8,000	126,080
4	256	160,000	13,495,040
5	1,024	3,200,000	1,569,745,920
6	4,096	64,000,000	192,780,943,360

## B. Progress Towards Major Research Goals

The project goals were to (1) prepare and investigate synthetic hosts that can distinguish between monosaccharides that differ only by the orientation of a single hydroxyl group, (2) determine how common elements of natural carbohydrate binding, including multivalency and cooperativity, could be employed in the context of synthetic lectins, (3) combine carbohydrate-compatible organic reactions with nanoscale site-specific molecular printing techniques, and (4) utilize carbohydrate-synthetic lectin interactions in the context of hierarchical assemblies. To address these goals, the binding mechanism and selectivity of a new mannose-selective receptor were explored (**Section C.1.**). The structure of this complex was determined by variable temperature and variable concentration  $^1\text{H}$  NMR spectroscopy, 2D NMR spectroscopy, and density functional theory (DFT) molecular modeling. By determining quantitatively all of the thermodynamic binding parameters ( $\Delta H^\circ$ ,  $\Delta S^\circ$ ,  $K_{\text{aS}}$ ), cooperativity was confirmed as an essential element of binding, and an unprecedented concentration-dependent switching was observed. Additionally, Polymer pen lithography (PPL), a molecular printing approach that uses arrays of polymeric tips, was used to covalently pattern glycans using various different organic transformations (**Section C.2.**). Finally, the motion of catalytic Au-Pt nanorods and their interactions with their environments was investigated so they can be used as essential element in hierarchical carbohydrate-directed nanostructure design (**Section C.3.**).

## C. Results and Discussion

### C.1 Synthetic Lectin Design

Natural saccharide-binding proteins, including lectins and periplasmic substrate-binding proteins, use water desolvation, hydrogen bonding (H-bonding), and C–H $\cdots\pi$  interactions to selectively recognize glycans that may differ only by the orientation of a single hydroxyl group to achieve binding affinities,  $K_a$ s, as high at  $10^6$  M $^{-1}$ . Selective carbohydrate recognition with artificial receptors remains a major area of investigation because of the challenge of differentiating between molecules with subtle structural differences, their ability to reveal fundamental aspects of saccharide binding, and their potential applications in disease detection, therapy, or catalysis. Mannose is a particularly interesting monosaccharide target because it is involved in signaling for several cancers, and as a consequence developing mannose specific synthetic receptors could reveal how carbohydrates are employed for communication purposes. However, synthetic carbohydrate receptors with increased binding affinity, expanded substrate scope beyond all-equatorial glycosides, and increased selectivity to levels comparable with their biological counterparts are still needed before these receptors become more widely utilized.

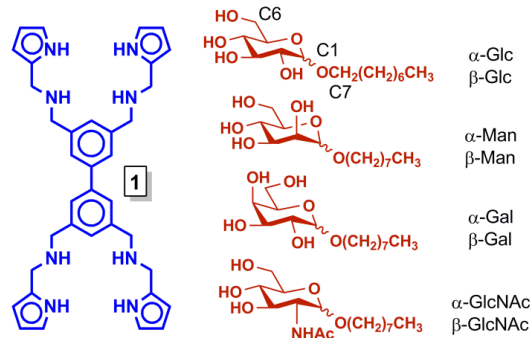


**Fig. 1** Structures of **1** (blue) and octyl pyranosides (red) whose binding with **1** was studied, with carbon numbering scheme.

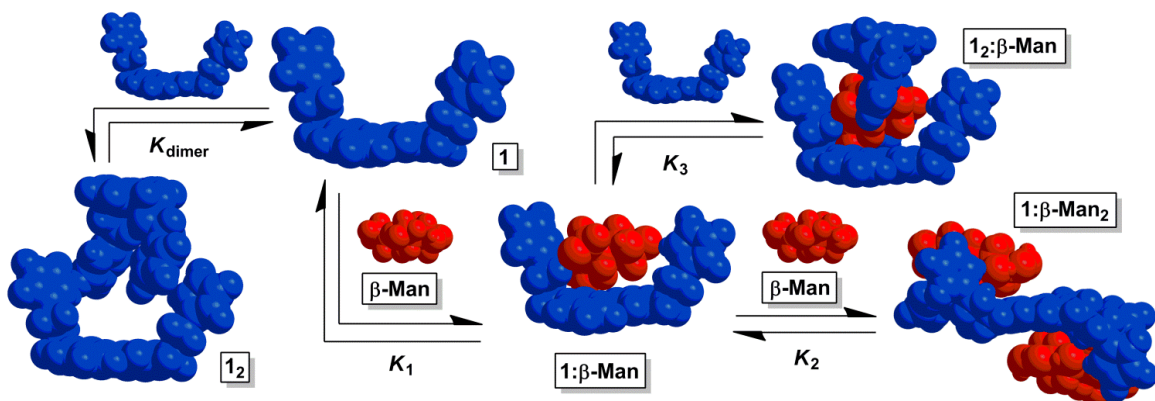


**Fig. 2** The equilibria present in a chloroform mixture of **1** and β-Man at 25°C. Upon increasing the β-Man:**1** ratio,  $K_2$  determines the dominant species in solution. If instead, β-Man:**1** decreases,  $K_3$  controls the equilibrium mixture.

To address these challenges, an alternate design approach towards synthetic saccharide receptors that involves preparing a flexible host that does not possess rigid preorganization and as a result is capable of binding carbohydrates through pathways that arise from conformational rearrangements and positive homotropic cooperativity was pursued (*Chem. Sci.* **2013**, *4*, 357-367). Homotropic cooperativity – whereby an initial association of a target substrate induces conformational restrictions that enhance further binding of the same substrate – has been employed previously in synthetic receptors to increase binding strength towards targets such as diacids and syn-diols. However, synthetic receptors that utilize homotropic cooperativity remain rare, and few examples exist of hosts that rely upon cooperativity to enhance saccharide binding, despite the fact that cooperativity and multivalency are ubiquitous elements of carbohydrate recognition in biology. The advantages that could arise with carbohydrate receptors that employ positive allosteric cooperativity include (1) shorter synthetic sequences because specificity and affinity are the direct result of allostery, (2) increased solubility associated with receptor flexibility, and (3) employing the same binding mechanisms as natural saccharide receptors could provide fundamental insights into the complex carbohydrate recognition motifs that are prevalent in nature. To this end, we have designed receptor **1** that contains aminopyrrolitic groups appended to a flexible scaffold with eight freely rotating methylene groups and a freely rotating biphenyl bond (Figure 1). Thus, **1** was designed to dynamically explore thermodynamic and

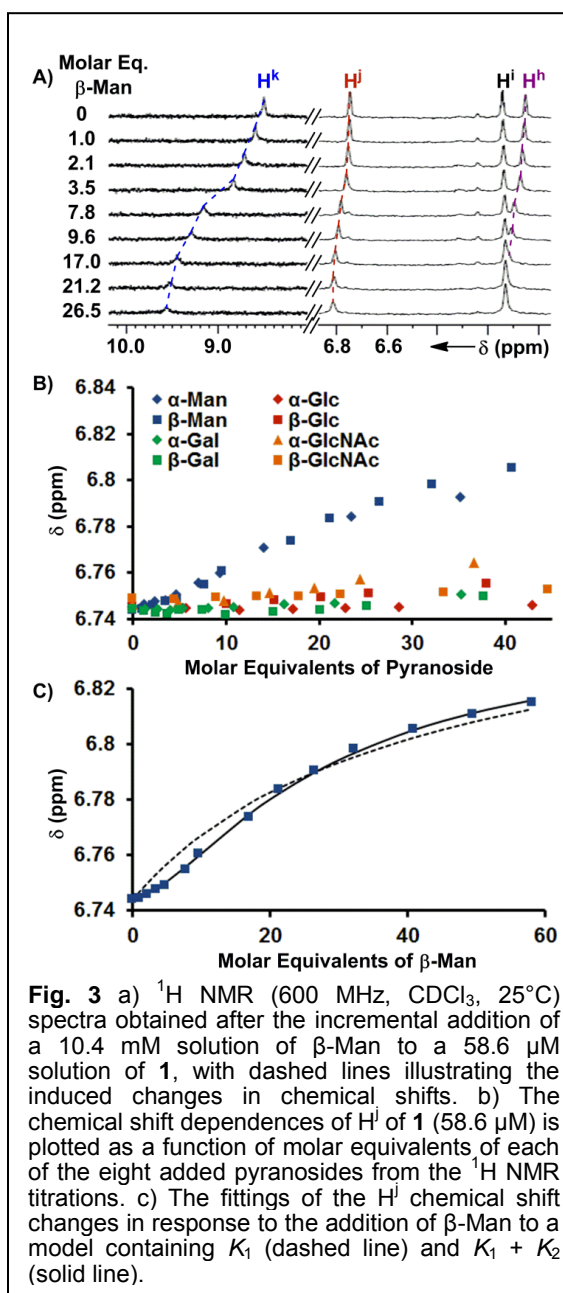


**Fig. 3** a) <sup>1</sup>H NMR (600 MHz, CDCl<sub>3</sub>, 25°C) spectra obtained after the incremental addition of a 10.4 mM solution of β-Man to a 58.6 μM solution of **1**, with dashed lines illustrating the induced changes in chemical shifts. b) The chemical shift dependences of H<sup>j</sup> of **1** (58.6 μM) is plotted as a function of molar equivalents of each of the eight added pyranosides from the <sup>1</sup>H NMR titrations. c) The fittings of the H<sup>j</sup> chemical shift changes in response to the addition of β-Man to a model containing K<sub>1</sub> (dashed line) and K<sub>1</sub> + K<sub>2</sub> (solid line).

conformational space and confirm that increased receptor flexibility can induce specificity for carbohydrate guests through allostery despite a higher entropic penalty experienced in an initial association step. Through the use of <sup>1</sup>H NMR titrations, we found that **1** achieves excellent selectivity for octyl mannosides through two allosteric cooperative pathways (Figure 2) with an overall selectivity as high as 16.8:1 α-Man:α-Gal in chloroform. Moreover, the selectivity is directly dependent on pyranoside concentration, where **1** binds preferentially to β-Glc at low

concentration (<0.3 mM), then binds  $\alpha$ - and  $\beta$ -Man at higher concentrations. **1** is the first synthetic carbohydrate receptor that (1) relies on cooperativity to increase selectivity and (2) whose selectivity switches with saccharide concentration.

### *Pyranoside binding*

Receptor **1** was prepared in a five step synthetic sequence in a 64% overall yield, and the binding affinity and selectivity of **1** for eight octyl pyranosides (Figure 1), which were chosen as guests because they are common terminal residues found on cell surface glycoconjugates and are used as standards for assaying synthetic receptor selectivity were investigated by variable temperature  $^1\text{H}$  NMR titrations in  $\text{CDCl}_3$ . Chloroform facilitates the binding studies of new carbohydrate receptors because the solvent does not compete for H-bonding between host and guest, thereby enhancing polar noncovalent bonds. These titrations revealed that the selectivity of **1** for octyl mannosides arises through a cooperative, multistep equilibrium (Figure 2). In solution, **1** exists as a dimer,  $\mathbf{1}_2$ , that comes apart to form 1:1 complexes with the eight pyranosides with little selectivity. Upon altering the **1**:pyranoside ratio from 1:1, two new mannose-selective binding modes emerge that are both the result of positive cooperativity at 25°C. When the concentration of mannose is increased, 1:2 receptor:pyranoside complexes form only with  $\alpha$ -Man (**1**: $\alpha$ -Man<sub>2</sub>) and  $\beta$ -Man (**1**: $\beta$ -Man<sub>2</sub>). If instead, the concentration of **1** increases with respect to pyranoside, a 2:1 receptor:monosaccharide complex forms only with  $\beta$ -Man ( $\mathbf{1}_2$ : $\beta$ -Man). To understand the origin of the preferential binding of mannoses by **1**, these binding stoichiometries and the structures of  $\mathbf{1}_2$ : $\beta$ -Man, **1**: $\alpha$ -Man<sub>2</sub>, and **1**: $\beta$ -Man<sub>2</sub> were established through a variety of 1D and 2D NMR methods, and all values of  $K_1$ ,  $K_2$ ,  $K_3$ ,  $\Delta H^\circ$  and  $\Delta S^\circ$  were determined for each of these equilibria.

### *1:2 Receptor:pyranoside binding*

The binding of pyranosides was first studied under conditions where receptor **1** was maintained at a low concentration (<70  $\mu\text{M}$ ) to minimize the contribution of the  $K_{\text{dimer}}$  and  $K_3$  equilibria (Figure 2). Once the values of  $K_1$  and  $K_2$  were determined, their values were held invariant in subsequent peak shift fittings, which facilitated the quantification of the other  $K_a$ s. The incremental addition of a

**Table 2.** Binding constants ( $K_a$ , 25°C) and thermodynamic parameters ( $\Delta H^\circ$ ,  $\Delta S^\circ$ ) associated with the 1:1 (upper value), 1:2 (middle value), and 2:1 (lower value) **1**:pyranoside binding stoichiometries determined by NMR titrations and the intrinsic median binding concentration  $BC_{50}^0$  calculated from  $K_{\text{dimer}}$ ,  $K_1$ ,  $K_2$ , and  $K_3$  for each pyranoside interacting with **1** in  $\text{CDCl}_3$  at 25°C.

Glycoside	Log $K$	$\Delta H^\circ$ (kcal mol <sup>-1</sup> )	$\Delta S^\circ$ (e.u.)	$BC_{50}^0$ (mM)
$\alpha$ -Glc	$2.75 \pm 0.04$	$-12.5 \pm 0.3$	$-29 \pm 1$	
	<i>a</i>	—	—	$1.86 \pm 0.16$
	<i>a</i>	—	—	
$\beta$ -Glc	$3.16 \pm 0.01$	$-16.5 \pm 0.1$	$-41 \pm 1$	
	<i>a</i>	—	—	$0.70 \pm 0.02$
	0.39 <sup>b</sup>	$-6.6 \pm 0.4$	$-21 \pm 1$	
$\alpha$ -Man	$2.57 \pm 0.19$	<i>c</i>	<i>c</i>	
	$3.71 \pm 0.10$	<i>c</i>	<i>c</i>	$0.46 \pm 0.05$
	<i>a</i>	—	—	
$\beta$ -Man	$2.46 \pm 0.31$	$-20.5 \pm 0.8$	$-57 \pm 3$	
	$3.34 \pm 0.11$	$-20.2 \pm 1.2$	$-52 \pm 4$	$0.73 \pm 0.10$
	2.45 $\pm 0.09$	$-11.0 \pm 0.4$	$-26 \pm 2$	
$\alpha$ -Gal	$2.18 \pm 0.02$	$-13.1 \pm 0.5$	$-34 \pm 2$	
	<i>a</i>	—	—	$7.74 \pm 0.31$
	<i>a</i>	—	—	
$\beta$ -Gal	$2.59 \pm 0.03$	$-15.4 \pm 0.8$	$-40 \pm 3$	
	<i>a</i>	—	—	$2.74 \pm 0.18$
	<i>a</i>	—	—	
$\alpha$ -GlcNAc	$2.53 \pm 0.02$	$-11.4 \pm 0.2$	$-26 \pm 1$	
	<i>a</i>	—	—	$3.18 \pm 0.14$
	<i>a</i>	—	—	
$\beta$ -GlcNAc	$2.65 \pm 0.05$	$-11.8 \pm 0.5$	$-27 \pm 4$	
	<i>a</i>	—	—	$2.37 \pm 0.26$
	<i>a</i>	—	—	

<sup>a</sup> No detectable binding. <sup>b</sup> Estimated by extrapolation of a van't Hoff plot with the assumption  $\Delta C_p = 0$ . <sup>c</sup> Not determined.

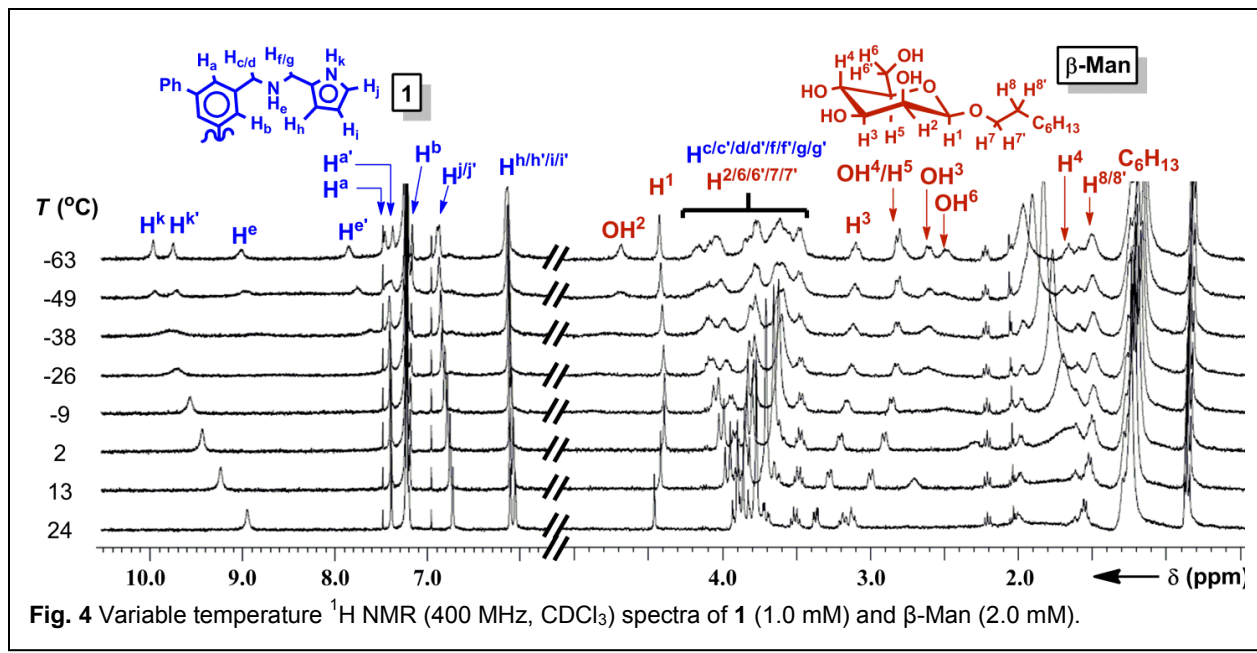


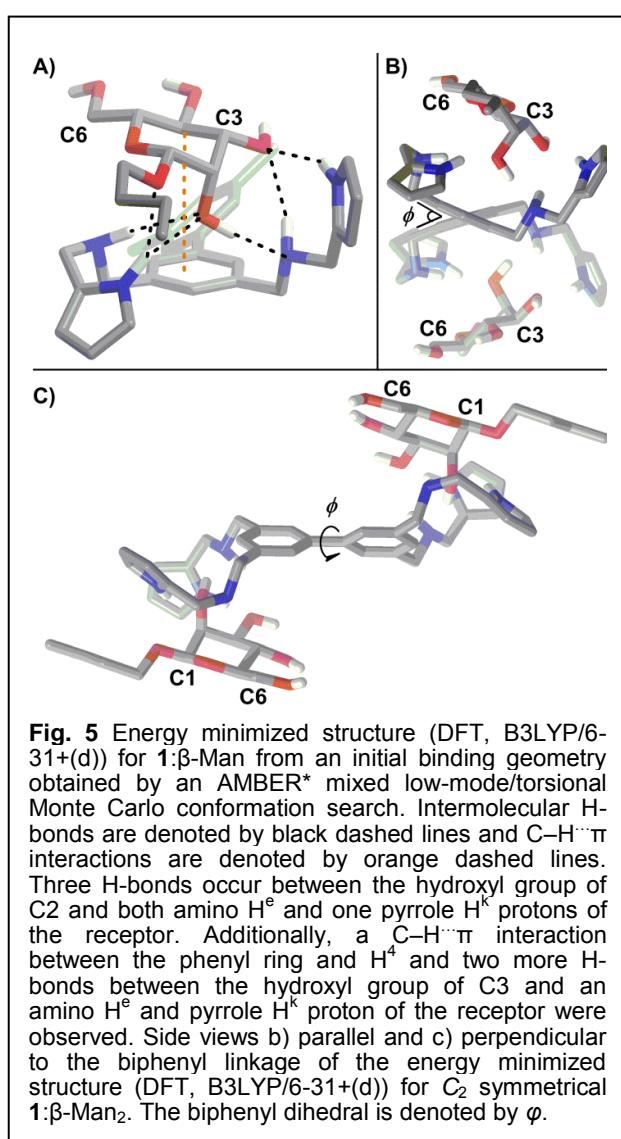
**Fig. 4** Variable temperature  $^1\text{H}$  NMR (400 MHz,  $\text{CDCl}_3$ ) spectra of **1** (1.0 mM) and  $\beta\text{-Man}$  (2.0 mM).

10–12 mM solution of each of the eight octyl pyranoside to a dilute solution of **1** (58.6  $\mu\text{M}$ ) induced changes in the  $^1\text{H}$  NMR chemical shifts corresponding to the protons of **1**, owing to a fast exchange between bound and unbound substrates on the NMR timescale (Figure 3A). Notably, the change of mannose proton chemical shifts,  $\Delta\delta$ , was significantly greater than the other pyranosides, suggesting that the overall binding free energy,  $\Delta G^\circ$ , was greater for mannoses than other pyranosides (Figure 3B). When the observed chemical shifts were plotted against the molar equivalents of pyranoside (Figure 3C), the observed perturbations for the mannose protons follow a sigmoidal pattern, indicating that multiple equilibria in addition to 1:1 complexation are occurring in the titration. The titration induced peak shifts occurring upon addition of both anomers of glucose ( $\alpha/\beta\text{-Glc}$ ), galactose ( $\alpha/\beta\text{-Gal}$ ), and N-acetylglucosamine ( $\alpha/\beta\text{-GlcNAc}$ ) produced no such sigmoidal curve and instead follow the hyperbolic shape of a 1:1 binding isotherm (Figure 3B). Since the concentration of pyranosides was intentionally kept low, the saturation region of the binding isotherm was only reached for the mannoses (Figure 3C), thus  $K_1$  could not be determined for the other pyranosides from these experiments, although we were able to obtain these values by titrating **1** into solutions of pyranoside.

The chemical shift changes that occur because of the interaction of **1** with  $\alpha$ - and  $\beta\text{-Man}$  were subjected to a global nonlinear fitting analysis with a model incorporating  $K_{\text{dimer}}$ ,  $K_1$ , and  $K_2$ , and satisfactory fits to the  $\Delta\delta$ s were obtained to provide macroscopic  $K_a$ s indicating the presence of 1:2 receptor:mannose complexes  $\mathbf{1}:\alpha\text{-Man}_2$  and  $\mathbf{1}:\beta\text{-Man}_2$ . For an allosteric receptor possessing two equivalent binding sites, the experimentally measured  $K_a$ s must be corrected for the existence of two identical 1:1 intermediates to obtain microscopic association constants that accurately describe the association of each binding site. Since there are two identical pathways by which  $\alpha/\beta\text{-Man}$  can associate with **1** to form a 1:1 complex, the macroscopic  $K_a$  for the first association process was divided by 2 to obtain microscopic association constant  $K_1$ . Likewise, as there are two identical pathways for dissociation in

**1:Man<sub>2</sub>**, the macroscopic  $K_a$  for the second association process was multiplied by 2 to obtain microscopic association constant  $K_2$  (Table 2). The interaction parameter,  $\alpha$ , is the ratio of a microscopic  $K_a$  in the presence of cooperativity over its value in the absence of cooperativity, or reference  $K_a$ , and is a quantitative measure of cooperativity. Since both binding sites are identical, the reference  $K_a$  is equivalent to  $K_1$  and thus  $\alpha = K_2 / K_1$ . An  $\alpha$  value greater than 1 indicates that the first association event enhances the second, i.e. positive cooperativity. Likewise, the binding is negatively cooperative if  $\alpha$  is less than 1, and the binding is non-cooperative if  $\alpha$  is equal to 1. From an analysis of the microscopic  $K_{as}$ ,  $\alpha$ -Man and  $\beta$ -Man were both found to possess  $\alpha$  values of 13.7 and 7.6 respectively with receptor **1**, indicating a high degree of positive cooperativity occurs between **1** and both mannosides (Table 2).

The thermodynamic origin of this positive allosteric cooperativity in the formation of **1:β-Man<sub>2</sub>** was investigated by determining  $\Delta H^\circ$  and  $\Delta S^\circ$  associated with each binding step. The <sup>1</sup>H NMR titrations between **1** and  $\beta$ -Man were repeated at 20, 15, and 10°C, and  $K_1$  and  $K_2$  values for each temperature were obtained and subjected to Van't Hoff analyses to provide the thermodynamic parameters associated with each binding event. Notably, the  $\Delta H^\circ$ 's of association for the first and second binding step are identical,  $-20.5 \pm 0.8$  and  $-20.2 \pm 1.2$  kcal mol<sup>-1</sup> respectively, suggesting that both equivalents of  $\beta$ -Man bind **1** with an identical number of noncovalent interactions and that the mannosides do not interact with each other when bound to **1**. A comparison of the corresponding  $\Delta S^\circ$  values indicates a decrease in the unfavorable  $\Delta S^\circ$  occurs in the second binding step compared to the first,  $-52 \pm 4$  and  $-57 \pm 3$  e.u. respectively.



The geometries of **1:β-Man** and **1:β-Man<sub>2</sub>** were determined by 1D and 2D <sup>1</sup>H NMR and computational modeling to understand the structural origin of the cooperative binding. The <sup>1</sup>H NMR spectrum of a solution of **1** (1 mM) and  $\beta$ -Man (2 mM) in CDCl<sub>3</sub> exhibits averaged signals for all protons at 25°C because of a fast exchange of the signals corresponding to **1**,  $\beta$ -Man, **1:β-Man<sub>2</sub>**, and **1:β-Man**. Upon cooling, the <sup>1</sup>H NMR resonances corresponding to **1**, except H<sup>b</sup>, decoalesce into two sets of peaks at -40°C

(Figure 4), indicating a partial desymmetrization occurring with receptor **1**. No decoalescence was observed for the resonances corresponding to  $\beta$ -Man signals upon cooling the solution (Figure 4), suggesting that both equivalents of  $\beta$ -Man occupy identical chemical environments in the **1:** $\beta$ -Man<sub>2</sub> complex. In the absence of  $\beta$ -Man, the signals corresponding to **1** in the <sup>1</sup>H NMR spectrum do not decoalesce at low temperature, but rather are broadened. Thus, the new signals that arise upon cooling of the mixed sample can be attributed to a complex consisting of **1** and  $\beta$ -Man. A comparison of the <sup>1</sup>H NMR spectra at -63°C with varying ratios of **1:** $\beta$ -Man revealed that the broad signals corresponding to free **1** disappear when more than two molar equivalents of  $\beta$ -Man are present in solution, further confirming the 1:2 stoichiometry of the complex. The two sets of signals observed in the <sup>1</sup>H NMR spectrum at -63°C (Figure 4) for the receptor and only one for the mannoside, indicate that both pyranosides are bound to two aminopyrrolitic arms of **1** and are symmetrically equivalent, resulting in a **1:** $\beta$ -Man<sub>2</sub> complex that exhibits C2 symmetry. A configuration where each mannose binds to two aminopyrrolitic arms on the same aromatic ring would render both H<sup>b</sup> protons of receptor **1** symmetrically equivalent. With NMR providing a general understanding of how  $\beta$ -Man sits within **1**, a molecular mechanics (AMBER\*) Monte Carlo conformational search was utilized to model the binding geometry of the **1:** $\beta$ -Man complex. The conformational searches yielded only one minimum energy structure for **1:** $\beta$ -Man, which was further optimized using density functional theory (B3LYP/6-31G+(d)). The resulting calculated structure (Figure 5A) is in excellent agreement with the experimental 1D <sup>1</sup>H NMR data.

The origin of the cooperativity in receptor **1** was examined computationally by varying the dihedral about the biphenyl bond ( $\varphi$ , Figure 5B/C) as this is the only dynamic element of the receptor that is shared by both binding sites. While desolvation contributes significantly to  $\Delta S^\circ$ , it is not the source of cooperativity as both binding sites and mannosides are solvated identically. A comparison of the DFT (B3LYP/6-31G+(d)) minimized structures corresponding to **1**, **1:** $\beta$ -Man, and **1:** $\beta$ -Man<sub>2</sub> revealed  $\varphi$  values of 40.2°, 38.5°, and 39.1° respectively, indicating that the contribution of torsional strain towards the observed cooperativity is negligible because  $\varphi$  in the bound state is close to the preferred  $\varphi$  of unbound **1**. More likely, the presence of a bound  $\beta$ -Man restricts the rotation about  $\varphi$  and incurs an entropic penalty that is only paid in the first

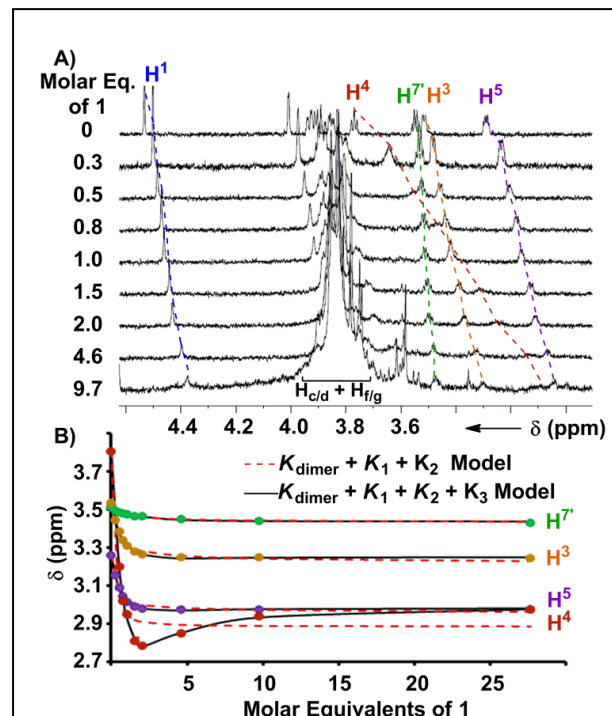


**Fig. 6** a) <sup>1</sup>H NMR (900 MHz, CDCl<sub>3</sub>, 25°C) spectra obtained upon the titration of a 62.5 mM solution of **1** to a 0.98 mM solution of  $\beta$ -Man with dashed lines illustrating the induced changes in  $\delta$ . b) Chemical shifts,  $\delta$ , of  $\beta$ -Man as a function of molar equivalents of **1** at 5°C. The theoretical global fits with a model incorporating  $K_{\text{dimer}}$ ,  $K_1$ , and  $K_2$  (dashed line) and with  $K_{\text{dimer}}$ ,  $K_1$ ,  $K_2$ , and  $K_3$  (solid line) are shown.

association.

#### 1:1 and 2:1 Receptor:pyranoside binding

The  $K_1$  and  $K_3$  of the binding of **1** to pyranosides were determined by titrating a solution of **1** (53.0 – 62.5 mM) into a 1.0 mM  $\text{CDCl}_3$  solution of each octyl glycoside until a large excess of **1** was reached. Addition of **1** produced considerable changes in the  $^1\text{H}$  NMR resonances of the receptor and all eight pyranosides (Figure 6A). For each non-mannoside,  $K_1$  was determined by subjecting all resolvable resonances from each titration at 25°C to a global nonlinear fitting analysis with a model combining  $K_1$  and  $K_{\text{dimer}}$  ( $13.0 \pm 0.5 \text{ M}^{-1}$ ) (Table 2). Likewise, when the observed upfield chemical shift changes associated with  $\alpha$ -Man were fit to a model incorporating  $K_{\text{dimer}}$  and the previously determined values of  $K_1$  and  $K_2$ , excellent fits for the peak shifts were obtained (Table 2). However, the peak shifts for the  $\beta$ -Man titration could only be fit accurately when the formation of a complex consisting of two molecules of **1** and one molecule of  $\beta$ -Man ( $1_2:\beta\text{-Man}$ , Figure 2) was considered (Figure 6B). The observed  $\Delta\delta$ s were fit to a model consisting of  $K_{\text{dimer}}$ ,  $K_1$ ,  $K_2$ , and  $K_3$ , with every binding constant except  $K_3$  held invariant, to determine  $K_3$  for  $\beta$ -Man. The values of  $\log K_1$  for binding between **1** and all pyranosides range from 2.5 to 3.3 with the highest values associated with  $\alpha$ - and  $\beta$ -Man and  $\beta$ -Glc. Importantly, little difference exists between the  $K_1$ s for the eight pyranosides, indicating that little selectivity occurs in the first binding event. In contrast to the modest selectivity found in  $K_1$ , 2:1 binding is only observed for  $\beta$ -Man at 25°C ( $K_3 = 282 \text{ M}^{-1}$ ), although a value of  $K_3 = 3 \text{ M}^{-1}$  for  $\beta$ -Glc can be extrapolated from a van't Hoff plot. Interestingly, a second receptor association does not occur with  $\alpha$ -Man suggesting that the octyl chain at the anomeric position, which would be orientated away from the biphenyl base of **1** in  $1:\alpha\text{-Man}$  (Figure 5A), interferes with the association of a second receptor.

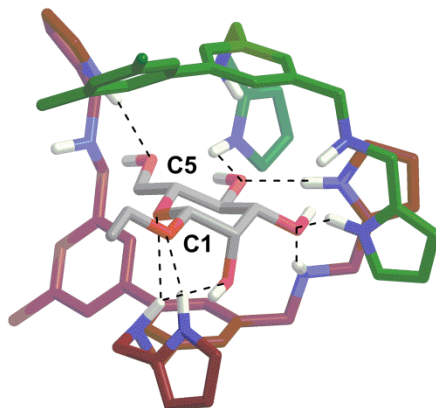


**Fig. 7** Energy minimized structure (AMBER\*) for  $1_2:\beta\text{-Man}$  obtained by a mixed low-mode/torsional Monte Carlo conformation search. The carbons of **1** that binds the  $\alpha$ -face are colored green, and the carbons of **1** bound to the  $\beta$ -face are colored red for clarity, nitrogens are blue, oxygens are red, and intermolecular hydrogen bonds are denoted by dashed lines. Upon the association of the second equivalent of **1**, 3 new H-bonds are observed with the  $\beta$ -face.

The cooperativity that facilitates the formation of  $1_2:\beta\text{-Man}$  can be understood through the interaction parameter,  $\alpha$ , which is the ratio between the values of  $K_3$  in the presence and in the absence of cooperativity, the latter being the reference  $K_a$ . Since the two faces of  $\beta$ -Man are inequivalent, the two receptors do not bind to identical sites, thus  $K_1$  is not an appropriate reference  $K_a$ . Rather, since  $K_3$  describes the binding of the  $\beta$ -face of  $\beta$ -Man, which contains  $\text{H}^1$ ,  $\text{H}^3$ , and  $\text{H}^5$ , in the presence of a receptor bound to the  $\alpha$ -face, which contains  $\text{H}^4$ , the reference  $K_a$  would describe the receptor binding to the  $\beta$ -face in the absence of a receptor bound to the  $\alpha$ -face. From the  $-63^\circ\text{C}$   $^1\text{H}$ - $^1\text{H}$  ROESY spectrum of  $1:\beta\text{-Man}_2$ , there are no observable NOEs between the pyranoside protons on the  $\beta$ -face and the biphenyl base of receptor **1**. Likewise, a ROESY spectrum performed at conditions that would produce significant quantities of the 1:1  $1:\beta\text{-Man}$

complex revealed only a NOE between H<sup>4</sup> of the  $\alpha$ -face and H<sup>a</sup>. Under these experimental conditions, a 1:1 binding event between **1** and the  $\beta$ -face does not occur to any appreciable extent, so an approximate baseline value of  $K_a \leq 104 \text{ M}^{-1}$  was obtained. Thus, an estimated  $K_3 \geq 282 \text{ M}^{-1}$  is evidence for positive cooperativity in  $K_3$  with  $\beta$ -Man, with a corresponding  $\alpha$  of at least 2.7.

To determine why  $K_3$  occurs exclusively with  $\beta$ -Man at room temperature,  $\Delta H^\circ$  and  $\Delta S^\circ$  of association for each binding event between **1** and all pyranosides were obtained by repeating the <sup>1</sup>H NMR titrations at 20, 15, 10, and 5°C and subjecting the resulting  $K_a$ s to van't Hoff analyses (Table 2). All monosaccharides fit satisfactorily to a  $K_{\text{dimer}} + K_1$  model at all temperatures, except for  $\beta$ -Man at all temperatures and  $\beta$ -Glc, at 15, 10, and 5°C, which required inclusion of the 2:1 receptor:pyranoside equilibrium ( $K_3$ ) to achieve satisfactory fits to the titration data. When comparing the thermodynamic parameters for the formation of each 1:1 complex, a decrease in  $\Delta H^\circ$  occurs with a decrease in magnitude of  $\Delta S^\circ$ , which can be rationalized within the context of enthalpy-entropy compensation. Notably, the two  $\beta$ -monosaccharides with the highest 1:1 binding enthalpies,  $\beta$ -Man and  $\beta$ -Glc, are the only pyranosides that participate in  $K_3$ . The large difference in  $\Delta H^\circ$  between 1: $\beta$ -Man and 1: $\beta$ -Glc, –20.5 and –16.5 kcal mol<sup>–1</sup> respectively, suggests that the high selectivity in  $K_3$  for  $\beta$ -Man is the result of **1** forming more noncovalent contacts with  $\beta$ -Man than with  $\beta$ -Glc, resulting in a more preorganized 1:1 complex. The  $\Delta H^\circ$ s for the formation of 1<sub>2</sub>: $\beta$ -Glc and 1<sub>2</sub>: $\beta$ -Man, –6.6 and –11.0 kcal mol<sup>–1</sup> respectively, suggest that significantly more noncovalent contacts are formed in the latter, indicating that the selectivity for  $\beta$ -Man in the second binding event is enthalpically driven.

The binding geometries of 1: $\beta$ -Man and 1<sub>2</sub>: $\beta$ -Man were determined and compared to understand how the preorganization of 1: $\beta$ -Man facilitates the formation of 1<sub>2</sub>: $\beta$ -Man. A <sup>1</sup>H-<sup>1</sup>H ROESY experiment that was performed under conditions that favor the 1:1 complex (1: $\beta$ -Man : 1: $\beta$ -Man<sub>2</sub> = 2 : 1.5) was consistent with the previously determined binding geometry for 1: $\beta$ -Man. Notably, in the 1: $\beta$ -Man geometry, a significant portion of  $\beta$ -Man is exposed to solvent because one of the arms of **1** is orientated downwards underneath the n-octyl chain of  $\beta$ -Man, which provides a window for a second equivalent of **1** to bind onto the exposed  $\beta$ -face of  $\beta$ -Man. The structure of 1<sub>2</sub>: $\beta$ -Man was determined by performing a <sup>1</sup>H-<sup>1</sup>H ROESY experiment with a concentrated 2:1

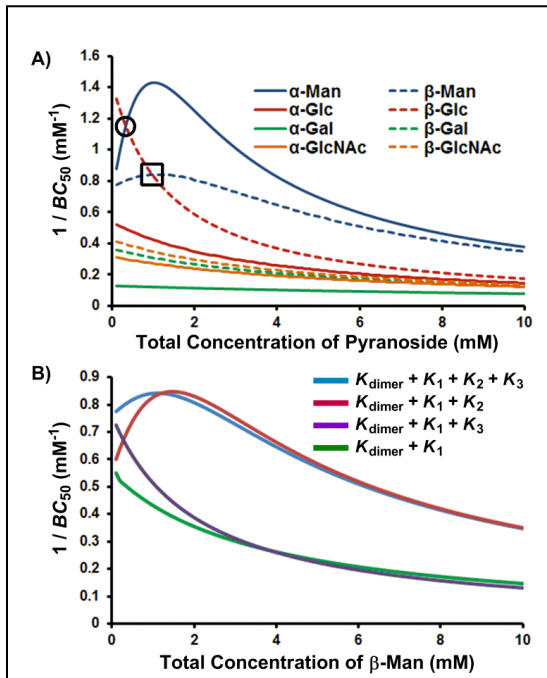


**Fig. 8** 1/BC<sub>50</sub> plots describing a) the pyranoside concentration dependence for the overall binding strength (1/BC<sub>50</sub>) of receptor **1** toward each pyranoside, where higher values are indicative of stronger binding and crossover points, marked within a circle for  $\beta$ -Glc →  $\alpha$ -Man and square for  $\beta$ -Glc →  $\beta$ -Man, denote changes in binding preference with increasing pyranoside concentration; and b) the influence of each positive cooperative binding equilibria ( $K_2$  and  $K_3$ ) on the BC<sub>50</sub> value of receptor **1** for  $\beta$ -Man.

receptor:pyranoside  $\text{CDCl}_3$  mixture at  $-10^\circ\text{C}$  where  $\mathbf{1}_2:\beta\text{-Man}$  would be the major species in solution. NOEs were observed between protons located on the biphenyl base and pyrroles, suggesting a geometry where one molecule of  $\beta\text{-Man}$  is encaged by two molecules of  $\mathbf{1}$ , and the two molecules of  $\mathbf{1}$  are in close contact. By using a similar AMBER\* conformational search that was used to obtain the  $\mathbf{1}:\beta\text{-Man}$  structure, a  $\mathbf{1}_2:\beta\text{-Man}$  structure was obtained (Figure 7) that is consistent with the thermodynamic data and the 1D and 2D  $^1\text{H}$  NMR spectra. In contrast, the  $^1\text{H}-^1\text{H}$  ROESY of  $\beta\text{-Glc}$  and  $\mathbf{1}$  under conditions that favor the 1:1 complex revealed that the axial protons on both faces of  $\beta\text{-Glc}$  have observable NOEs with the biphenyl base of  $\mathbf{1}$ , indicating that more than one binding geometry exists at equilibrium since  $\mathbf{1}$  cannot interact with both faces of  $\beta\text{-Glc}$  simultaneously. Because the entropic penalty for the preorganization of  $\mathbf{1}:\beta\text{-Glc}$  has not been paid, we speculate that the  $\Delta S^\circ$  associated with a second molecule of  $\mathbf{1}$  binding to the 1:1 complex becomes prohibitively high, preventing the formation of a 2:1 complex. It should be noted that in the calculated structure of  $\mathbf{1}_2:\beta\text{-Man}$  only three arms of each equivalent of  $\mathbf{1}$  participate in binding to  $\beta\text{-Man}$ , so the fourth arms can be replaced in future receptors to increase function.

#### *Implications of competing equilibria on the selectivity of $\mathbf{1}$*

In the presence of  $\beta\text{-Man}$ , the 1:1 complex,  $\mathbf{1}:\beta\text{-Man}$ , can either bind a second molecule of pyranoside, to form  $\mathbf{1}:\beta\text{-Man}_2$  ( $K_2$ ), or  $\mathbf{1}$ , to form  $\mathbf{1}_2:\beta\text{-Man}$  ( $K_3$ ). The outcome of these two competing processes is dependent on the concentrations of each substrate, with  $K_2$  dominating at high concentrations of  $\beta\text{-Man}$  relative to  $\mathbf{1}$ , whereas  $K_3$  is preferred in the presence of excess  $\mathbf{1}$ . Thus, the numerous equilibria operating simultaneously in a solution of  $\mathbf{1}$  and pyranoside ( $K_{\text{dimer}}$ ,  $K_1$ ,  $K_2$  and  $K_3$ ) and the concentration dependence of cooperative binding complicate the analysis of the overall selectivity of  $\mathbf{1}$  for the eight pyranosides. The  $\text{BC}_{50}$  values of each of the pyranosides – defined as the total concentration of receptor  $\mathbf{1}$  needed to bind 50% of the available pyranosides in solution – were computed over a pyranoside concentration range of 0 to 10.0 mM to probe both the magnitude and concentration dependence of the selectivity of  $\mathbf{1}$  for the eight pyranosides (Figure 8A). Note that all equilibria present in a receptor/pyranoside mixture contribute toward the calculated  $\text{BC}_{50}$  value, and a higher  $1/\text{BC}_{50}$  value is indicative of a higher overall binding strength.

The  $1/\text{BC}_{50}$  plots reveal the effects of positive cooperativity on the binding affinity of  $\mathbf{1}$  toward mannosides. Molecules with  $K_2$  possess parabolic curves in the  $1/\text{BC}_{50}$  plot. This is particularly evident for  $\alpha\text{-Man}$  which possesses the highest affinity for  $\mathbf{1}$  compared to all other pyranosides at a 0.8 mM pyranoside concentration. Interestingly, for  $\beta\text{-Man}$ , which exhibits cooperativity in both  $K_2$  and  $K_3$ , a broader parabolic shape is observed, and little concentration dependence on the overall binding strength occurs between 0 and 4.0 mM of  $\beta\text{-Man}$ . When the calculated  $1/\text{BC}_{50}$  plot is compared to a hypothetical plot in which only  $K_1$  and  $K_3$  are present, it was found that the presence of  $K_3$  induces a substantial increase in selectivity at low concentrations (< 1.5 mM) of  $\beta\text{-Man}$  (Figure 8B). Alternatively, when a hypothetical plot is generated with only  $K_1$  and  $K_2$ ,  $K_2$  enhanced selectivity when  $[\beta\text{-Man}]$  is greater than 1.0 mM, thus demonstrating the direct contribution of cooperative, complex equilibria on selectivity in saccharide receptors (Figure 8B). Moreover, these plots confirm that pyranoside concentration controls which equilibrium, i.e.  $K_2$  or  $K_3$ , prevails. At concentrations below 1.0 mM of  $\beta\text{-Man}$ ,

higher stoichiometry binding is achieved through  $K_3$ , while at greater  $\beta$ -Man concentrations,  $K_2$  dominates.

As each  $1/BC_{50}$  plot is a measure of affinity between **1** and pyranosides, comparing the plots of two or more pyranosides provides a means of assessing selectivity. Thus, the concentration of  $\alpha$ -Man where the maximum  $1/BC_{50}$  value is obtained (0.8 mM) is also where the maximum selectivity occurs for  $\alpha$ -Man relative to the other pyranosides. Beyond this value, the selectivities gradually approach 2:1 mannoside:pyranoside, which is a consequence of the differences in binding stoichiometry – receptor **1** can accommodate two molecules of mannosides and only binds 1:1 for the other pyranosides. Importantly, crossover points in the  $BC_{50}$  plots are observed between  $\beta$ -Glc and the mannosides (Figure 8A), *meaning that the selectivity of **1** changes as a function of pyranoside concentration*. At low pyranoside concentrations (< 0.3 mM), receptor **1** binds  $\beta$ -Glc with the highest affinity owing to its high value of  $K_1$ , which effectively competes with the cooperative binding of **1** toward mannosides. From 0.3 mM to 1.0 mM, the binding order for **1** is  $\alpha$ -Man >  $\beta$ -Glc >  $\beta$ -Man. At higher pyranoside concentrations (> 1.0 mM), the binding order for **1** changes to  $\alpha$ -Man >  $\beta$ -Man >  $\beta$ -Glc as a result of the 2:1 binding stoichiometry that occurs only with mannosides. Consequently, a new concentration dependence has been discovered that governs the stoichiometry of the resulting complex and the pyranoside preference of the receptor.

#### *Significance and outlook*

The flexible receptor **1** achieves selectivity between pyranosides that may differ only by the orientation of a single hydroxyl group, despite the entropic penalty that must be paid to organize the complexes. In fact, the lack of preorganization in the strong **1**: $\beta$ -Glc complex precludes the formation of a stable **1**<sub>2</sub>: $\beta$ -Glc structure, so entropy contributes significantly towards selectivity. Although receptor **1** does not achieve the same overall affinity as the best rigidly preorganized mannose-specific receptors, the selectivity is comparable despite the differences in binding mechanisms, thus confirming the hypothesis that increasing the receptor dynamics reveals new binding geometries because of the ability of flexible hosts to dynamically explore conformational space.

Synthetic carbohydrate receptors can provide insight into the subtleties of natural lectin-carbohydrate interactions and reveal how carbohydrate recognition conveys complex information in biological networks. Eukaryotic cell surfaces are coated with a carbohydrate layer, the glycocalyx, where the multivalent presentation of carbohydrates on a cell surface enhances binding affinity, a phenomenon termed the cluster glycoside effect. Interestingly, the selectivity of **1** changes with pyranoside concentration, where **1** preferentially binds glucosides at low concentration (<0.3 mM) and mannosides at higher concentrations that are similar to the increased localized concentrations present in mannoside clusters on cell surfaces. While concentration dependent selectivity may be unprecedented with synthetic carbohydrate receptors, multivalency and cooperativity are ubiquitous in biology, so concentration dependent switching may commonly occur with natural lectins and could have implications for hierarchical organization and information transfer in biological networks. This work (*Chemical Science*, 2013, 4, 357–367) represents the accomplishment of the major program goals with respect to

synthetic lectins by creating a new receptor that engages cooperativity, a binding mode ubiquitous to natural lectins, to perform molecular logic operations.

### C.2. New Surface Chemistries for Glycan Microarrays

Microarrays consisting of biologically active probes (proteins, antibodies, oligonucleotides, etc.) immobilized onto a solid support have revolutionized biology, have led to breakthroughs in biomedical research, and are now employed clinically to determine treatment courses for various diseases. Glycomics, an emerging area of biology that aims to understand the role of carbohydrates, glycolipids, and glycoproteins (glycans) in disease, could benefit greatly from the widespread use of microarrays. In the context of this grant, new lithography methods to create nanoscale features of carbohydrates with precise control over glycan density and orientation for subsequent hierarchical assembly with synthetic lectins have been developed. The orientation of glycans in arrays is important because binding affinities ( $K_a$ s) between sugars and lectins are typically low ( $10^2 - 10^3 \text{ M}^{-1}$ ) and having a high surface density of oriented glycans is critical for appreciable binding. However, common immobilization strategies do not deposit all probes in an active orientation, so the  $\text{Cu}^{\text{l}}$  catalyzed azide-alkyne cycloaddition (Cuaac) (*Small*, **2012**, *8*, 2000-2005) and the Staudinger Ligation (*Chem. Commun.* **2012**, *48*, 4995-4997) have been combined with Polymer Pen Lithography (PPL) to create functional glycan arrays.

The Cuaac is a powerful reaction for immobilizing biological probes because the alkyne and azide functional groups are bioorthogonal, the reaction proceeds quickly and in

high yield, and as a result it has been adopted widely by researchers for applications in chemical biology, materials science, and nanotechnology. Moreover, the Cuaac is increasingly seen as a solution to the challenge of orientation and immobilization in glycan arrays. As a result, there is a need for new patterning tools that can substantially reduce the amount of materials required to print glycan arrays and can site-specifically induce the formation of carbohydrate-compatible surface reactions

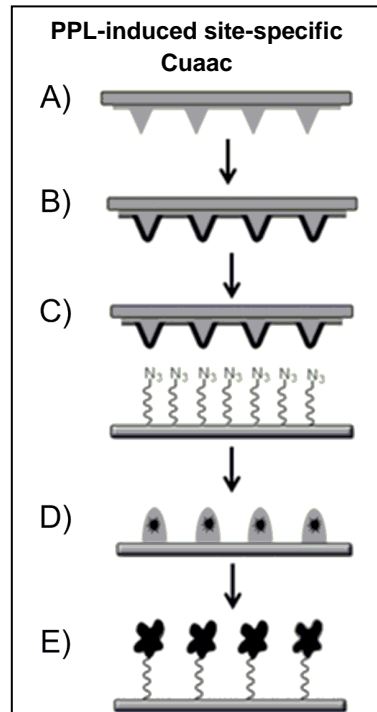


**Figure 9.** A) A PPL tip-array. B) The PPL tip-array coated with an ink mixture consisting of alkyne, PEG,  $\text{Cu}^{\text{l}}$ -catalyst, and reducing agent. C) The inked tip array is brought into contact with an azido-terminated surface to form patterns. D) The PEG nanoreactors are left on the surface so the Cuaac reaction can proceed. E) Following rinsing of the surface to remove the PEG, only the covalently immobilized molecules remain patterned onto the surface.

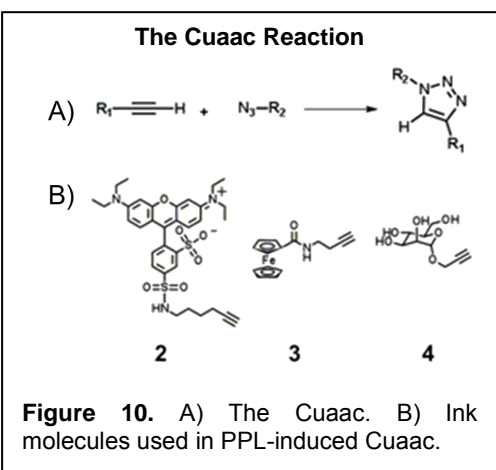
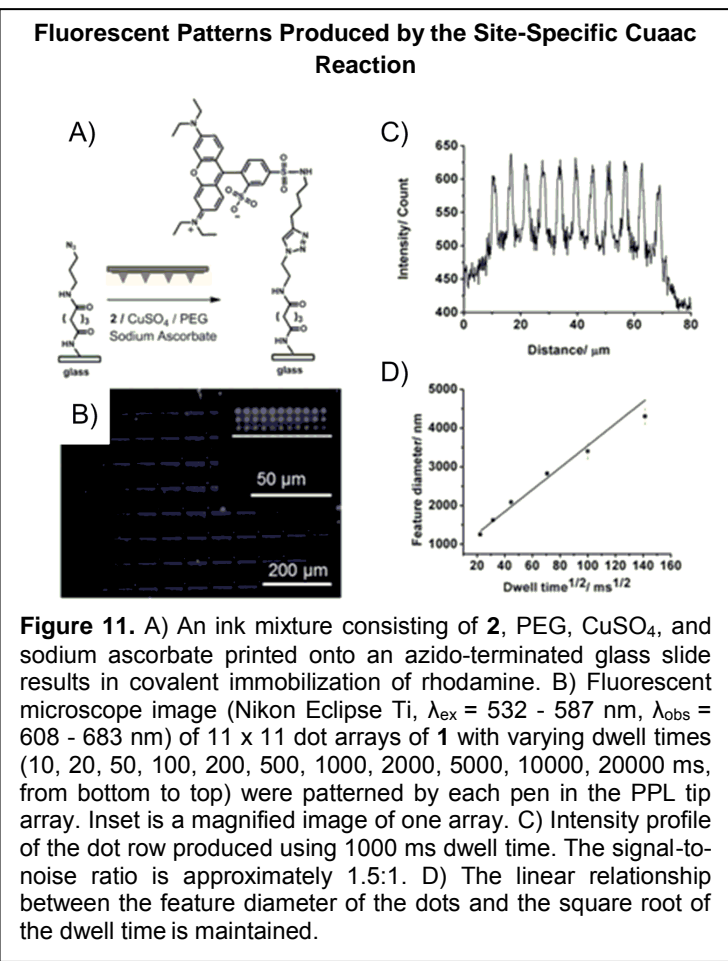


**Figure 10.** A) The Cuaac. B) Ink molecules used in PPL-induced Cuaac.

like the CuAAC. Conventional microarraying tools, like pin-printing or droplet-deposition, cannot readily produce sub-50  $\mu\text{m}$  diameter features that would minimize the usage of difficult to obtain carbohydrate samples. Microcontact printing ( $\mu\text{Cp}$ ) and Dip-pen nanolithography (DPN) are two popular molecular printing methods to create sub-1  $\mu\text{m}$  diameter features without denaturing or damaging delicate organic and biologically active probes.  $\mu\text{Cp}$  employs elastomeric stamps with photolithographically predefined patterns to transfer inks to surfaces, but the materials properties of the elastomers used to fabricate the stamps impose constraints that limit the array pattern, and  $\mu\text{Cp}$  is not readily multiplexed. DPN is a scanning-probe based molecular printing strategy that prepares arbitrary patterns of features with diameters as small as 15 nm and has been used to pattern lipids, proteins, and DNA, but its low-throughput and the necessity to optimize the transport of each new ink through the aqueous meniscus limits its utility. PPL is a promising molecular printing technique that employs arrays of as many as  $10^7$  elastomeric tips, and the precise spatial control of the piezoelectric actuators of an atomic force microscope (AFM) enable nanometer scale feature resolution over  $\text{cm}^2$  areas. Like DPN, the pens are coated with an ink, and the ink is transferred from the tips to the surface through an aqueous meniscus, with feature sizes ranging from 80 nm to over 100  $\mu\text{m}$ . Importantly, PPL has already been used to print multiplexed antibody arrays, where different inks are deposited simultaneously by each tip. As a consequence, PPL could solve the challenges associated with printing glycan arrays by significantly reducing feature diameters if it can simultaneously implement carbohydrate compatible surface immobilization reactants.



However, combining the surface chemistries required to form glycan arrays in a high quality and reproducible fashion using tip-based lithographies has been particularly challenging because of idiosyncrasies unique to these printing methods. In DPN and PPL the aqueous meniscus that is the conduit for ink transport from the tip to the surface and enables precise control over feature diameter also increases the difficulty of performing site-specific organic reaction on surfaces because the various entities involved in the reactions must move through the meniscus together. To circumvent the

challenges that arise from differences in solubilities and diffusion rates between the components in the ink mixtures, several solutions have been devised such as indirect surface activation, or the use of metal coated tips within fluid cells. While these examples are important proof-of-concept demonstrations, the total area patterned is limited to  $100 \mu\text{m}^2$ , and because these techniques are not scalable, they do not provide a viable approach to the challenge of producing microarrays. Before tip-based nanolithography microarray fabrication can be realized, methods to site-specifically induce useful surface chemistry over large areas must be developed and validated.

In the context of this grant, carbohydrates and other soft molecules were immobilized successfully onto azido-functionalized glass and gold surfaces (Figure 9) to obtain features of fluorescent and redox-active inks with diameters as small as 200 nm across  $\text{cm}^2$  areas by combining PPL with the Cuaac. The utility of this technique in glycomics was validated by measuring the activity of a glycan array. To demonstrate that PPL could simultaneously deliver all the components necessary for the Cuaac to a surface and print reproducible patterns, fluorescent (**2**) and redox-active (**3**) alkyne-containing inks (Figure 9) were transferred by PPL onto azido-terminated surfaces, and the reactions were confirmed by fluorescence microscopy and electrochemical methods. Azide-terminated glass surfaces for fluorescence experiments were prepared from amino-coated glass slides (Arrayit Corp., USA), and azide-terminated Au surfaces were prepared by immersing freshly evaporated Au films (200 nm Au / 50 nm Cr) in an ethanolic solution of 11-azido-undecane-1-thiol for 24 h.

In PPL and DPN, differences in solubility and diffusion in the aqueous meniscus necessitates optimizing the patterning conditions for each ink and precludes the deposition of certain inks altogether. In the Cuaac, the alkyne, Cu<sup>I</sup> catalyst, and the reducing agent must arrive at the surface simultaneously and in specific ratios. In matrix-assisted polymer pen lithography (MA-PPL) inks are encapsulated within a poly(ethylene glycol) (PEG) transport matrix, and herein is employed to bring the various reactive components to the surface simultaneously to produce uniform patterns. Moreover, the PEG capsule deposited onto the surface maintains the dimensions of the printed feature and prevents the ink from

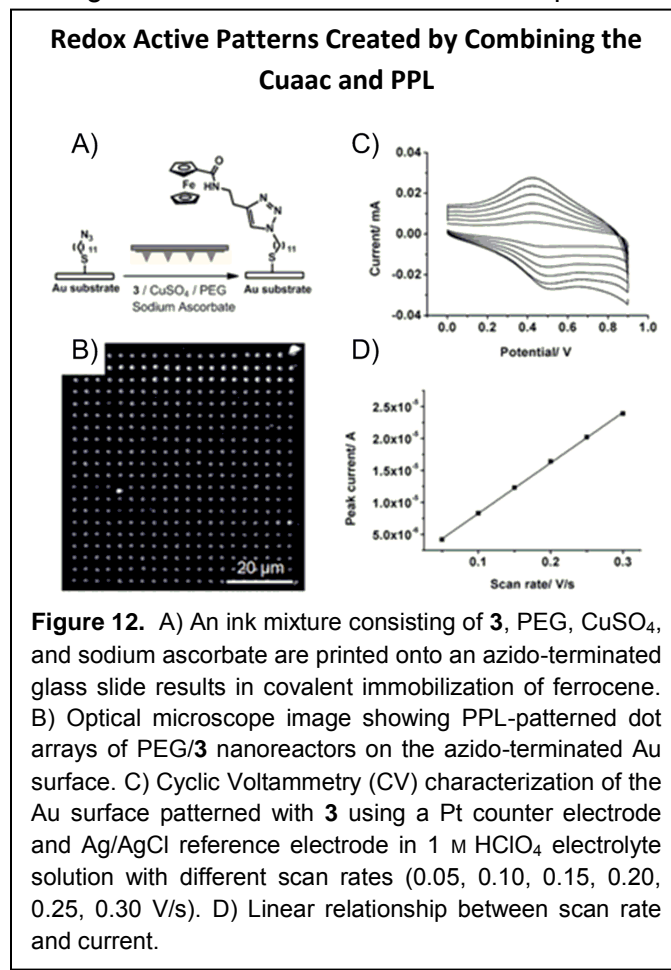


**Figure 12.** A) An ink mixture consisting of **3**, PEG, CuSO<sub>4</sub>, and sodium ascorbate are printed onto an azido-terminated glass slide results in covalent immobilization of ferrocene. B) Optical microscope image showing PPL-patterned dot arrays of PEG/**3** nanoreactors on the azido-terminated Au surface. C) Cyclic Voltammetry (CV) characterization of the Au surface patterned with **3** using a Pt counter electrode and Ag/AgCl reference electrode in 1 M HClO<sub>4</sub> electrolyte solution with different scan rates (0.05, 0.10, 0.15, 0.20, 0.25, 0.30 V/s). D) Linear relationship between scan rate and current.

spreading, which would otherwise increase the resulting feature diameter, while the CuAAC proceeds. To create a fluorescent pattern, **2**, CuSO<sub>4</sub>, ascorbic acid, and PEG were spin coated onto the 8000-pen PPL tip arrays and printed onto the azide-terminated glass surface into 11 x 11 dot patterns with the dwell-times varying from 10 – 20,000 ms at 80 – 85% humidity (Figure 11A). Optical and non-contact AFM microscopy confirmed the deposition of the PEG features and the uniformity of the patterns across the arrays. The PEG nanoreactors were left on the surface for 16 h so the reaction could proceed to completion. The PEG reactors were washed from the surface with H<sub>2</sub>O (10 mL) and EtOH (10 mL), and the size of the remaining fluorescent features of **2** were measured by fluorescence microscopy (Figure 11B). The signal-to-noise values for these dots range from 1.5 – 1.7 regardless of feature size, which is consistent with a monolayer of fluorophores (Figure 11C), and the linear relationship between feature size and dwell time is followed (Figure 11D). Control experiments, where no CuSO<sub>4</sub> was added to the ink mixture or the mixture was deposited onto an amino-terminated monolayer did not show any measurable fluorescence following washing, confirming that **2** was immobilized onto the surface as a result of the CuAAC and that the reaction does not occur unless all components necessary for the CuAAC reaction to proceed were present.

Electrochemical methods further demonstrated that the alkyne-containing inks were immobilized covalently onto the surfaces as a result of the CuAAC reaction (Figure 12A). Ink solutions comprised of **3**, CuSO<sub>4</sub>, PEG, and sodium ascorbate were patterned into 20 x 20 dot arrays by each tip in the 8000 pen array with an identical dwell time of 10 s for each dot, resulting in approximately  $2.7 \times 10^6$  features cm<sup>-2</sup>. Optical microscopy and AFM (Figure 12B) confirmed the uniformity of the pattern over large (1 mm – 100 μm) and small (<100 μm) length scales, respectively. These PEG nanoreactors had an average diameter of  $1.36 \pm 0.18$  μm calculated from 10 patterns randomly distributed across the array. After 16 h, the surface was washed with H<sub>2</sub>O (10 mL) and EtOH (10 mL) to remove excess ink, and EDTA (1 mM, aq, 10 mL) to remove excess Cu, leaving only molecules immobilized covalently onto the surface. The patterned surface was then immersed in an 80:20 EtOH: H<sub>2</sub>O solution of 1-hexyne (1.5 mM), CuSO<sub>4</sub> (0.1 mM), and sodium ascorbate (0.2 mM, 10 mL) for 16 h to passivate any unreacted azides, and the surfaces were subsequently washed with H<sub>2</sub>O (10 mL), EtOH (10 mL), and EDTA (1 mM, aq, 10 mL).

The large numbers of redox-active moieties by this approach enables quantification of the surface structure by electrochemical methods. Cyclic voltammetry (CV) was carried out in a custom built Teflon bore surface cell with an area of 0.38 cm<sup>2</sup>, a Ag/AgCl reference electrode, and a Pt counterelectrode in HClO<sub>4</sub> (1 M, aq) electrolyte solution (Figure 12C). The presence of the ferrocene (fc)/ ferrocenium (fc<sup>+</sup>) reversible redox couple from **3** was observed ( $E^\circ = 430$  mV vs Ag/AgCl), thereby confirming the presence of **3** on the surface. The peak of **3** is shifted anodically from fc because of the electron withdrawing amide linker between the fc and the alkyne of **3**. The CV was repeated at different scan rates, and the linear relationship between scan rate and maximum peak current (Figure 12D) confirms that **3** is covalently immobilized onto the surface. By integrating the peak current of the cyclic voltammograms, the surface coverage density of **3** within the features could be quantified.

A density of  $5.8 \pm 0.3 \times 10^{13} \text{ cm}^{-2}$  was determined. For comparison, surfaces were prepared with monolayer coverage of **3** by exposing the azide-terminated Au surfaces to a solution containing **3**, CuSO<sub>4</sub>, and ascorbic acid. Following electrochemical analysis, a  $\Gamma_{\text{fc}}$  value of  $7.3 \pm 0.1 \times 10^{13} \text{ cm}^{-2}$  was obtained, indicating that the PEG nanoreactors do not inhibit the progression of the CuAAC reaction.

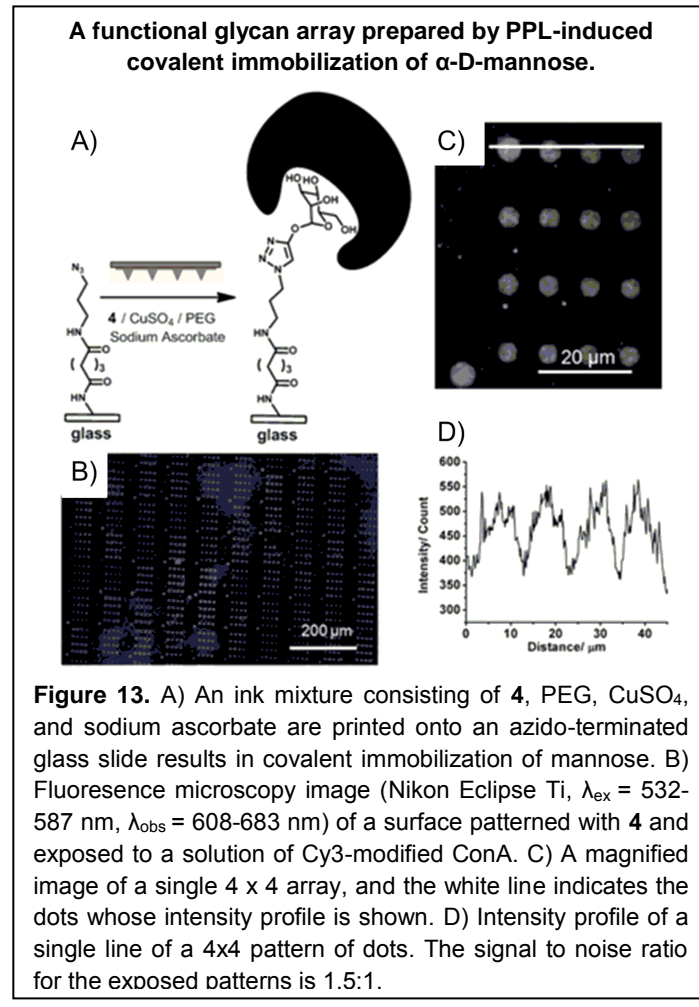


**Figure 13.** A) An ink mixture consisting of **4**, PEG, CuSO<sub>4</sub>, and sodium ascorbate are printed onto an azido-terminated glass slide results in covalent immobilization of mannose. B) Fluorescence microscopy image (Nikon Eclipse Ti,  $\lambda_{\text{ex}} = 532\text{-}587 \text{ nm}$ ,  $\lambda_{\text{obs}} = 608\text{-}683 \text{ nm}$ ) of a surface patterned with **4** and exposed to a solution of Cy3-modified ConA. C) A magnified image of a single 4 x 4 array, and the white line indicates the dots whose intensity profile is shown. D) Intensity profile of a single line of a 4x4 pattern of dots. The signal to noise ratio for the exposed patterns is 1.5:1.

printed at 80% humidity with a dwell time of 20 s. Subsequently, 4 x 4 patterns of **4** were printed onto azido-terminated glass surfaces, resulting in  $4.2 \pm 0.2 \mu\text{m}$  diameter features, calculated from 10 patterns across the array, that are large enough to resolve by either fluorescence microscopy or a conventional plate reader. The variation among features arises from tilting of the pen array with respect to the surface during writing or from minor differences in tip radii. Following printing, the pattern was immersed in a solution of bovine serum albumin (BSA) to passivate the unmodified azides on the surface. Concanavalin A (ConA) is an  $\alpha$ -mannose specific lectin that binds with a  $K_a$  of  $5 \times 10^6$  on a surface and is often used as a standard to confirm the activity of glycan arraying techniques. The surface was immersed in a solution of Cy3-modified ConA (0.5 mg/mL) for 5 h and washed three times with aqueous phosphate buffer (10 mM, pH 7.4, 0.005% Tween 20) to remove any protein that adhered nonspecifically to the

To demonstrate that the patterns produced by combining PPL with the CuAAC reaction can be used to create functional hierarchical structures, arrays of alkyne functionalized  $\alpha$ -D-mannose (**4**) were prepared (Figure 13A).  $\alpha$ -D-Mannose is a monosaccharide that is over expressed on the surface of certain cancer cells and the AIDS virus, and the ability to measure the interaction between  $\alpha$ -D-mannose and proteins in microarrays as a function of density could reveal how not only chemical composition affects hierarchical assembly in biology, but density dependent binding could also be employed in synthetic nanotechnology. Detecting binding to **4** was used as a proof-of-concept to demonstrate the utility of this patterning technique. **4** was prepared in two steps following previously reported literature protocols. To print the glycan arrays, **4** (100 mM), PEG (5 mg/mL), CuSO<sub>4</sub>, and sodium ascorbate were spin coated onto an 8000 pen PPL array and

surface. Upon imaging of the surface by fluorescence microscopy ( $\lambda_{\text{ex}} = 532 - 587 \text{ nm}$ ,  $\lambda_{\text{obs}} = 608-683 \text{ nm}$ ), the  $4 \times 4$  patterns of ConA bound to **4** were clearly observable across the  $\text{cm}^2$  area of the surface (Figure 13B, C). The signal to noise ratio of these features ranged from 1.4 - 1.8 (Figure 13D), which is in the same range found upon deposition of fluorophores directly onto surfaces. Importantly, exposure of the  $\alpha$ -D-mannose-patterned surface to Cy3 labeled glycoprotein, a protein that does not bind  $\alpha$ -D-mannose, did not result in any observable patterns, showing that the activity of these arrays is consistent with glycan arrays prepared by conventional methods.

### Matrix-Assisted PPL induced Staudinger Ligation

The Staudinger Ligation is a commonly used reaction to covalently link fluorescent molecules with biological substrates, resulting in the formation of amide bonds. The Staudinger Ligation has been investigated as a reaction for making microarrays of biologically active probes, although so far only with large spot sizes ( $> 50 \mu\text{m}$ ). However, the sensitivity of the phosphine to oxidation and the low-water solubility of aryl-phosphines have prevented the use of this reaction in molecular printing. For these reasons, the Staudinger Ligation was chosen to demonstrate the generality of matrix-assisted PPL (MA-PPL) as a reproducible tool for inducing site-specific organic reactions with 1-micrometer scale feature diameters and to show how fluorescent and redox active probes can be used as a facile method to characterize the success of the reaction (Figure 14).

Phosphine containing ink molecules **5** and **6**, equipped with fluorescent and redox-active labels, respectively, were prepared to confirm that the Staudinger Ligation could be employed to create patterns in the context of a MA-PPL experiment. To prepare **5**, rhodamine B base was reacted with 1-methyl-2-(diphenylphosphino)terephthalate and 2-(1H-7-Azabenzotriazol-1-yl)-1,1,3,3-tetramethyluronium hexafluorophosphate methanaminium (HATU) as a coupling agent, and **5** was isolated in 34% yield. To prepare redox-active ink **6**, ferrocene methanol was reacted with 1-methyl-2(diphenylphosphino)terephthalate and *N,N*-dicyclohexylcarbodiimide (DCC) (Figure 14C), and **6** was isolated in 34% yield. Both **5** and **6** were characterized by  $^1\text{H}$ ,  $^{13}\text{C}$ , and  $^{31}\text{P}$  NMR spectroscopies and high-resolution mass spectrometry, and all spectra were consistent with the proposed structures. The azido-terminated glass and gold surfaces were prepared following literature protocols. To create fluorescent patterns by MA-PPL induced

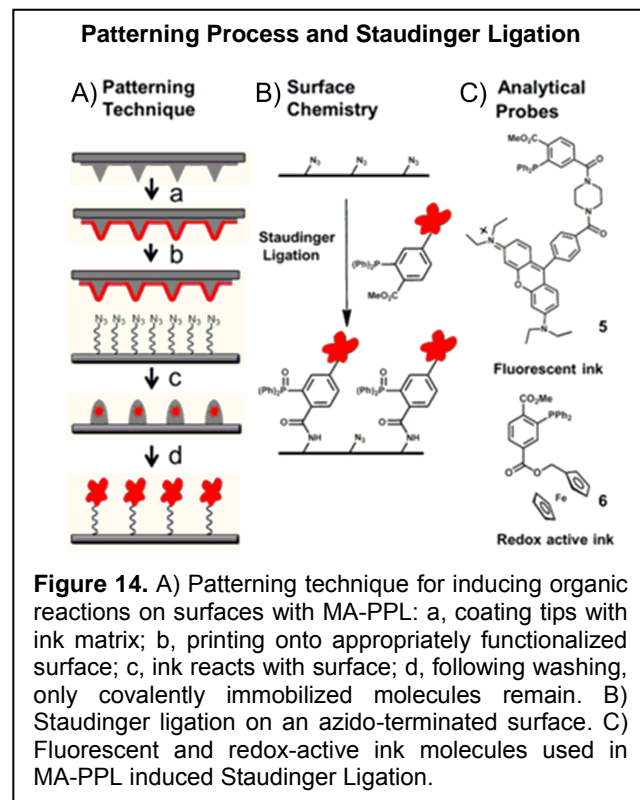


**Figure 14.** A) Patterning technique for inducing organic reactions on surfaces with MA-PPL: a, coating tips with ink matrix; b, printing onto appropriately functionalized surface; c, ink reacts with surface; d, following washing, only covalently immobilized molecules remain. B) Staudinger ligation on an azido-terminated surface. C) Fluorescent and redox-active ink molecules used in MA-PPL induced Staudinger Ligation.

Staudinger Ligation, an 8500-tip array with a tip-to-tip spacing of 80  $\mu\text{m}$  were made by following literature procedures and then exposed to O<sub>2</sub> plasma (Harrick PDC-001, 30 s, medium power) to render the surfaces of the pen-arrays hydrophilic prior to inking. Subsequently, four drops of the ink solution, comprised of **5** (1.3 mg, 1.5 mmol) and PEG (2000 g mol<sup>-1</sup>, 2.5 mg mL<sup>-1</sup>) in 2 mL 80:20 THF:H<sub>2</sub>O, which was sonicated to ensure solution homogeneity, were spin coated (2000 rpm, 2 min) onto the PPL array. The inked tips were mounted onto an atomic force microscope (AFM), the humidity was raised to 75 - 85%, and 8 x 8 dot arrays with dwell times ranging from 20 to 20000 ms were patterned. The ink mixture was left on the surface for 48 hr, and the surfaces were subsequently washed with THF and H<sub>2</sub>O.

Following washing, the fluorescent images were readily observable and showed control of feature size ranging from 1.49 to 2.68  $\mu\text{m}$ . A uniform pattern was prepared over the cm<sup>2</sup> area covered by the tip array (Figure 15). Moreover, the signal to noise value for these dots in the pattern ranges from 1.5 to 1.6 (Figure 16A), which is consistent with fluorophore monolayers and a linear relationship between dwell time and feature size is observed (Figure 16B), demonstrating the ability of PPL to control feature diameter precisely. The PEG matrix is vital to the uniform covalent immobilization of ink **5** on the solid substrate. Because of the poor solubility of

**5** in the aqueous meniscus that forms between the tip and the surface, no patterns formed in the absence of the PEG matrix. No fluorescent pattern was observed in the control experiment where ink **5** was printed onto an amino terminated glass slide, confirming that fluorescent patterns were only produced because the Staudinger Ligation proceeded successfully and site specifically on the azido-terminated surface. To characterize the ink density within each patterned feature, 20 x 20 dot arrays of **6** were patterned with each tip and with a dwell time of 10 s onto an azido-terminated gold surface following the same printing procedure described above. The uniform patterns over cm<sup>2</sup> area covered by the tip array were observed by optical microscopy (Figure 17). After 48 h of reaction, the excess ink was washed from the surface with THF and EtOH. To confirm the presence of the redox active species, cyclic voltammetry (CV) was carried out on the patterned surface using a custom built Teflon bore surface cell with an area of 0.38 cm<sup>2</sup>. A strong redox peak at  $E^\circ = 510$  mV (vs Ag/AgCl) is indicative of the presence

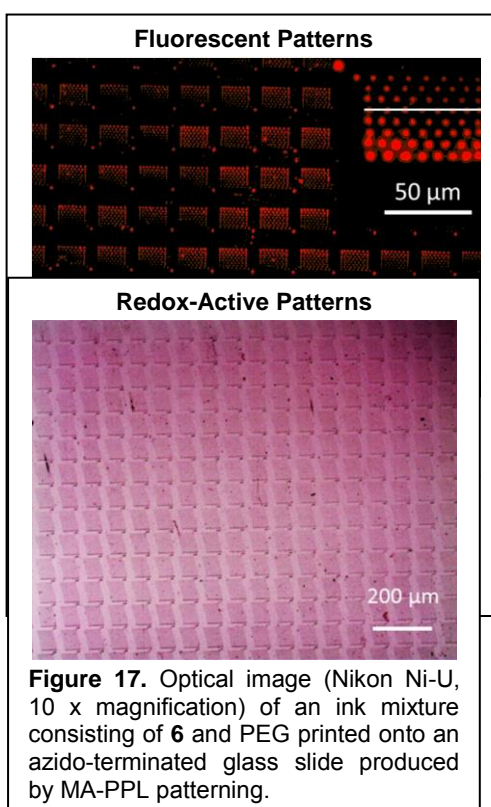


**Figure 17.** Optical image (Nikon Ni-U, 10 x magnification) of an ink mixture consisting of **6** and PEG printed onto an azido-terminated glass slide produced by MA-PPL patterning.

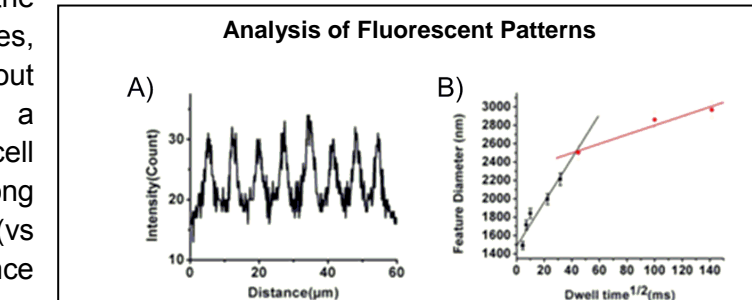


**Figure 16.** A) Intensity profile of the dot row produced using 0.5 s dwell time (indicated by the line in Fig. 9, inset). The signal-to-noise ratio is approximately 1.5:1. B) The linear relationship between the feature diameter of the dots and the square root of the dwell time is maintained, with saturation at high dwell times, as previously observed.

of the ferrocene (fc) / ferrocenium (fc<sup>+</sup>) reversible redox couple from **6** (Figure 17A). The anodic shift of the peak from fc is the result of the electron withdrawing ester bound to the ferrocene ring of **2** (Figure 17A). The linear relationship between peak current and scan rates was obtained by repeating CV measurements at different potential scan rates (Figure 17B), confirming the formation of stable amide bonds on the azido-terminated gold surface.

The surface density of fc within each feature,  $\Gamma_{fc}$ , was determined from the CV measurements using Eq. 1. A  $\Gamma_{fc}$  of  $1.99 \pm 0.03 \times 10^{14} \text{ cm}^{-2}$  was obtained, which was close to the theoretical maximum cover density of a self-assembled monolayer of fc species in a self-assembled monolayer —  $2.7 \times 10^{14} \text{ cm}^{-2}$ . A  $\Gamma_{fc}$  of  $2.23 \pm 0.02 \times 10^{14} \text{ cm}^{-2}$  was calculated when the azido-terminated gold surface was immersed in the THF solution of **6**, rather than patterning by PPL, indicating the reaction proceeds to nearly quantitative yield.

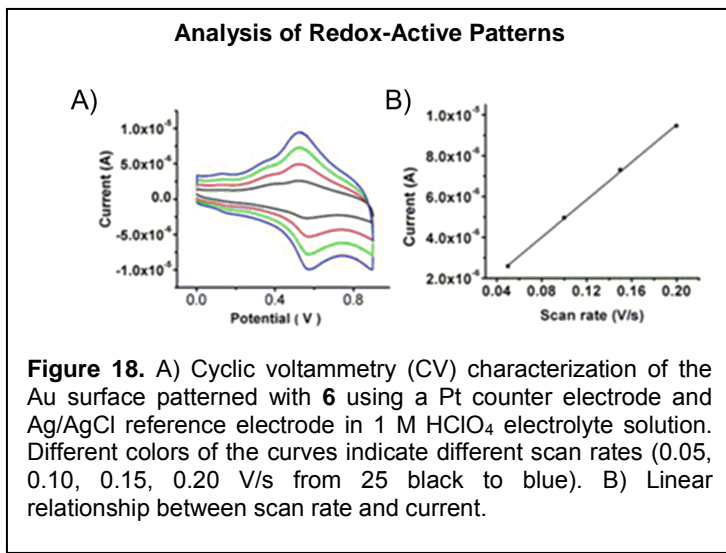


**Figure 18.** A) Cyclic voltammetry (CV) characterization of the Au surface patterned with **6** using a Pt counter electrode and Ag/AgCl reference electrode in 1 M HClO<sub>4</sub> electrolyte solution. Different colors of the curves indicate different scan rates (0.05, 0.10, 0.15, 0.20 V/s from 25 black to blue). B) Linear relationship between scan rate and current.

of binding between synthetic-lectins and their carbohydrate binding partners have been investigated, but other nanostructures could be combined with these systems, including autonomic synthetic nanomotors as a model for biological locomotion and assembly. Scientists are envisioning a future where synthetic nanomachines perform numerous tasks, including biosensing and drug delivery in medicine, flow control and mixing in microfluidics, and cargo transport and assembly in nanotechnology. To create dynamic nanosystems that incorporate carbohydrate lectin binding, the interactions and dynamics of all the individual components in isolation must first be understood. A prototype motor is a nanorod made of gold (Au) and platinum (Pt) segments that can be driven catalytically in hydrogen peroxide (H<sub>2</sub>O<sub>2</sub>) by a local flux of ions, which arises because of two paired redox reactions on the metal surfaces. Since the gold portion of nanorods allow the immobilization of either synthetic lectins or oligosaccharides onto a surface, the motions of catalytic nanorods can potentially be controlled by interactions between these two substrates. Various trajectories with linear, circular, and wavelike patterns have been reported for nanorods before, but it is not clear exactly how and why nanorods actively translate, rotate, and follow paths of different form. The trajectories must be predicted in order to fulfill the potential of synthetic motors through efficient design, control, and operation.

### C.3. Catalytically Propelled Nanorod Dynamics

Already, the thermodynamics

The dynamics of Au-Pt nanorods, namely their directional changes, displacement, and diffusion over time have been characterized, explained, and predicted (*Phys. Rev. Lett.* **2013**, *110*, 038301). Understanding these properties is critical to understanding the behavior over time of complex nanosystems. Nanorods of total length  $L = 2.0 \pm 0.2 \mu\text{m}$  and diameter  $2R = 0.39 \pm 0.04 \mu\text{m}$  (Figure 19A and 19B), with varying proportions of Pt ( $X$ ), were fabricated by electrochemical deposition in anodic aluminium oxide (AAO) templates using a previously reported method. Dilute suspensions of noninteracting nanorods were observed to move primarily in two dimensions with their axis parallel to a microscope slide. The location of each moving particle was tracked over time to analyze its trajectory (Figure 19C). Nanorods with equal portions of Au and Pt ( $X = 0.5$ ) were studied extensively because varying  $X$  does not change their speed, except for nearly pure Au and Pt, which decline in speed because the flux of ions is limited by the smaller catalytic surface area. We speculated that only a small region at the interface of Au and Pt is driving the motion, while the two end regions are merely contributing to the drag, which is consistent with longer nanorods moving more slowly. The speed  $U^*$  was controlled by varying the  $\text{H}_2\text{O}_2$  concentration ( $C$ ) because  $U^*$  increases approximately linearly with  $C$ , not only below 6% as previously reported, but up to 25%.

As the speed increases to  $\sim 40 \text{ ms}^{-1}$ , the underlying deterministic motion emerges from thermal noise and the tendency to move in circular paths is revealed (Figure 18D). The number of complete CCW turns (turning number) either increases or decreases at a comparable rate along each trajectory (Figure 19A), indicating that nanorods tend to move in circles with occasional switching between CW and CCW turns. Those moving in smaller circles, corresponding to trajectories with larger curvatures, typically spend more time turning in one sense before switching (Figure 19B).

The observed trajectory patterns were justified theoretically by calculating the expected path of a particle with minor asperities. For simplicity, we considered a wire of constant curvature  $\bar{\kappa}$  with a prescribed slip velocity on a proportion of the body, which is predicted to follow a curved path with comparable curvature  $\kappa \sim \bar{\kappa}$ . Figure 20A shows a sketch of such a wire with curvature  $\bar{\kappa} = 0.12 \mu\text{m}^{-1}$ , the median of the distribution of  $|\kappa|$  in Figure 20B. The gravitational potential energy is minimal near a surface in two stable configurations: one moving in CW turns

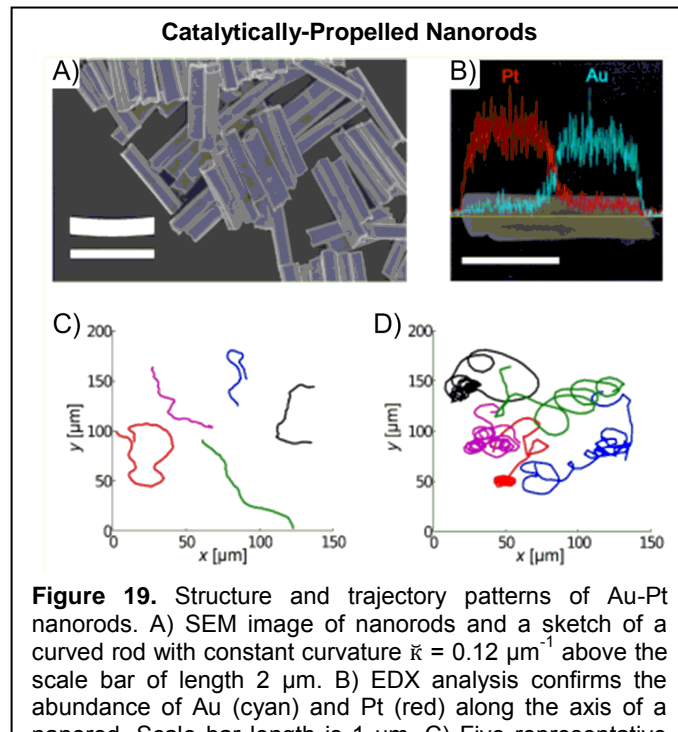


**Figure 19.** Structure and trajectory patterns of Au-Pt nanorods. A) SEM image of nanorods and a sketch of a curved rod with constant curvature  $\bar{\kappa} = 0.12 \mu\text{m}^{-1}$  above the scale bar of length  $2 \mu\text{m}$ . B) EDX analysis confirms the abundance of Au (cyan) and Pt (red) along the axis of a nanorod. Scale bar length is  $1 \mu\text{m}$ . C) Five representative trajectories of nanorods ( $X = 0.5$ ) tracked over 15 s in  $C = 3\%$ . D) Nanorods in  $C = 25\%$  move faster and tend to follow circular paths.

and the other in CCW turns (Figure 20C). To switch configurations, the bent body must flip by overcoming an energy barrier proportional to  $e^{mg\Delta h/k_B T}$ , where  $k_B$  is the Boltzmann constant,  $T$  is room temperature,  $m$  is the mass,  $g$  is the gravitational acceleration, and  $\Delta h \sim \kappa L^2/24$  is the minimum required change in elevation of the centre of mass. The flipping frequency is predicted by Equation 3

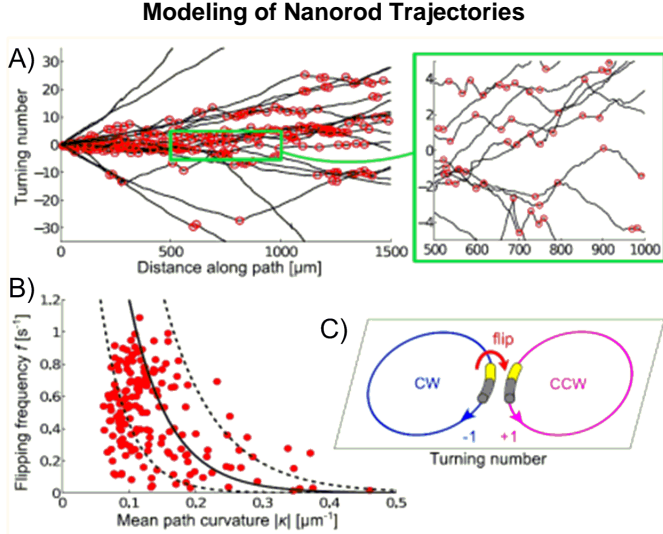


**Figure 20.** A) Number of CCW turns completed along 20 representative trajectories of nanorods ( $X = 0.5$ ) in  $C = 25\%$  (average speed  $\sim 40 \mu\text{m s}^{-1}$ ) tends to change at a steady rate with occasional switching of sign as marked by open circles. B) Trajectories with more curvature switch handedness less frequently. The theoretical curve (solid line) and the error bands (dashed lines) are given by equation (2). C) Sketch of bent nanorods flipping between turning left and right.

surface. The bend in the body shape, as well as a non-axisymmetric slip velocity arising possibly on the body surface, are referred to as asperities inducing the nanorods to deviate from following a straight path.

The microscopic motion involving turns and flips importantly dictates the macroscopic spreading of nanorods over long times, as predicted in our mathematical model formulated below. Consider the two-dimensional movement of rods with translational and rotational diffusion coefficients  $\bar{D}$  and  $D_r$  respectively, neglecting the difference in translational diffusion along and across the rod axis for simplicity. In the absence of thermal agitation, each rod is assumed to translate with speed  $U$  in the axial direction denoted by unit vector  $\mathbf{n} = (\cos \theta, \sin \theta)$ , and rotate with angular speed  $U_\kappa$ . The rods tend to follow paths with curvature  $\kappa = \pm \kappa_0$ , where the sign switches at a characteristic rate  $f$ . The centre of mass  $x = (x, y)$ , the orientation angle  $\theta$ , and the curvature  $\kappa$  are evolved in constant time steps of  $\Delta t$  according to the stochastic equations of motion,

$$(3) \quad x(t + \Delta t) - x(t) = U\mathbf{n}[\theta(t)]\Delta t + \sqrt{2\bar{D}\Delta t}X$$

$$(4) \quad \theta(t + \Delta t) - \theta(t) = U\kappa(t)\Delta t + \sqrt{2D_r\Delta t}X_3$$

$$(5) \quad \kappa(t + \Delta t) - \kappa(t) = -2\kappa(t)Y$$

$$(2) \quad f = f_0 e^{-mg\Delta h/k_B T}$$

where  $f_0 \sim 6.4 \text{ s}^{-1}$  was computed from the time scale of rotational diffusion about the long axis of a prolate spheroid with the same dimensions as the nanorods. Equation 2 predicts more curved trajectories to flip handedness less frequently, in agreement with experimental data (Figure 20B). A minor bend, as sketched in Figure 19A, is sufficient for suppressing the flipping frequency by an order of magnitude compared to a perfectly straight body because of the small distance  $k_B T/2mg \sim 10 \text{ nm}$  between the nanorods and the bottom

where  $\mathbf{X} = (X_1, X_2), X_3 \sim N(0,1)$  are independent random variables with a standard normal distribution, and  $Y \sim B(1, f\Delta t)$  is a Bernoulli random variable with success probability  $f\Delta t$ . 100 particles were simulated by varying the speed  $U$  systematically and fixing all other parameters based on estimates from the experiments (Table 3). The expected changes in orientation and position of the particles after any time are predicted by analytical solutions derived from the Fokker-Planck equation.

The theoretical predictions agreed quantitatively with our experimental data reported herein, which can be explained only by incorporating the effects of asperities. Our model predicts the correlation in orientation of nanorods to decay in time, with oscillations emerging at higher speeds, in good agreement with our experiments (Figure 21A). The typical time elapsed before changing orientation is given by the persistence time (Figure 21B), which is comparable at lower speeds but decreases systematically with smaller error bars at higher speeds. The reason is that slower nanorods change direction stochastically because of thermal agitation, while faster nanorods change direction more rapidly and deterministically by following circular paths. The persistence length (Figure 21C) is almost independent of speed because the circular paths have similar curvature.

Thermal agitation causes the nanorods to spread over time and space, in excellent agreement with our model. A measure of the area covered in time  $t$

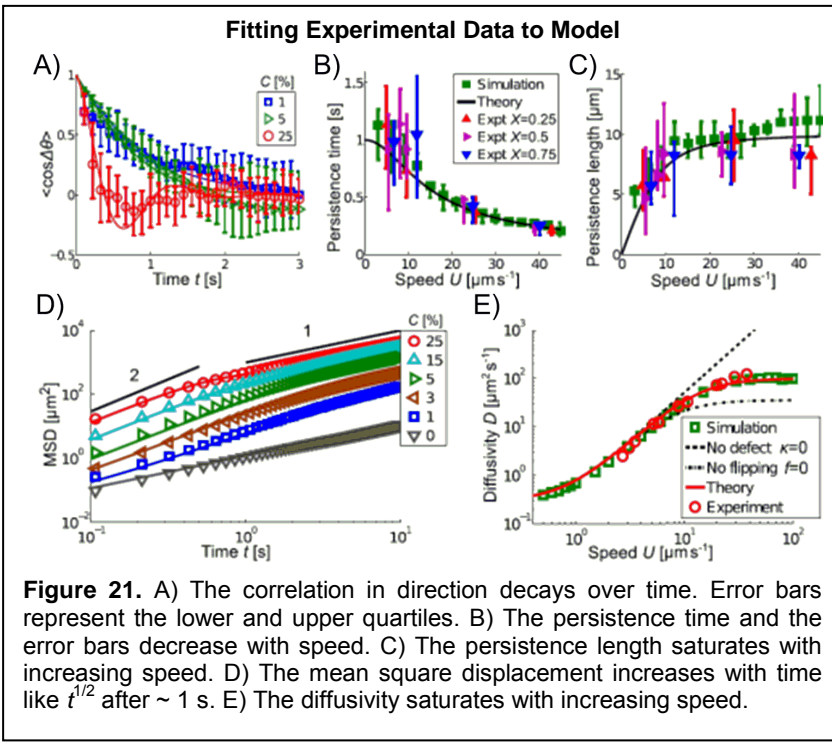


**Figure 21.** A) The correlation in direction decays over time. Error bars represent the lower and upper quartiles. B) The persistence time and the error bars decrease with speed. C) The persistence length saturates with increasing speed. D) The mean square displacement increases with time like  $t^{1/2}$  after  $\sim 1$  s. E) The diffusivity saturates with increasing speed.

through dispersion is given by the mean square displacement (MSD), as plotted on logarithmic scales in Figure 21d. Active nanorods follow quasi-ballistic trajectories over short intervals. Passive nanorods over any period and active nanorods over periods longer than about a second are diffusive, as indicated by the MSD evolving like  $4Dt$ , where  $D$  represents the diffusivity. Contrary to previous theories, the diffusivity saturates with increasing speed  $U$  (Figure 21E) and agrees well with our prediction:

$$(6) \quad D = \bar{D} + \frac{U^2(D_r+2f)}{2U^2\kappa_0^2+2D_r(D_r+2f)}$$

which is derived by incorporating the effects of asperities. In the absence of asperities ( $k_0 = 0$ ), the diffusivity is predicted to increase indefinitely with speed, consistent with the previous theories. In the absence of flipping ( $f = 0$ ), the diffusivity reduces to that of Brownian motion in circles. Neither of these theoretically idealized cases has been observed experimentally.

**Table 3. Fixed parameters in our theoretical model and simulations.**

Symbol	Parameter	Value
$D$	Translational diffusion coefficient ( $\mu\text{m}^2 \text{s}^{-1}$ )	$0.3 \pm 0.05$
$D_r$	Rotational diffusion coefficient ( $\text{s}^{-1}$ )	$1 \pm 0.4$
$K_0$	Absolute path curvature ( $\mu\text{m}^{-1}$ )	$0.12 \pm 0.04$
$f$	Flipping frequency ( $\text{s}^{-1}$ )	$0.9 \pm 0.5$

asperity significantly changes the trajectory patterns and diffusivity at higher speeds. Imperfections around the axis of motor movement should be reduced as much as possible if the general tendency to deviate from a straight path is undesirable. Sufficiently fast motors will move in circles and not result in efficient transport unless the tendency to turn is compensated by frequent flips. Motors with highly asymmetric shapes like rotors are less mobile and have a lower risk of escaping to other regions. Trajectories of particles with other shapes can be predicted by extending our model and evolving the curvature  $\kappa$  differently.

It is worth appreciating that some motile microorganisms behave in a similar way to these asymmetrically-shaped synthetic motors, despite differences in the mechanism of motility. Flagellated bacteria like *Escherichia coli* tend to swim in circles near a surface because of the helical shape of their flagella. Gliding organisms like the crescent-shaped body of *Toxoplasma gondii* move in circles as well, but can also follow a more linear path by flipping the body repeatedly, much like the movement of the nanorods described here. The small-scale motion along curved paths is ubiquitous in both synthetic and biological motility patterns, and strongly influences the large-scale diffusive behavior over long times. Importantly, the theoretical model described herein accounts for the movement of dynamic nanostructures over long times, which can be employed subsequently to predict the behavior and organization of carbohydrate-synthetic lectin dynamic nanosystems.

### C.5. Summary of Accomplishments

In summary, this award from the AFOSR has directly supported several major research accomplishments that led to the creation of carbohydrate-based nanotechnology. Specifically, we have created a synthetic lectin that employs cooperativity to obtain selectivity for mannose and characterized the thermodynamics of binding and the structure of this receptor when bound to several monosaccharides. *This work is a major breakthrough because, while cooperativity is ubiquitous in the binding of carbohydrates in nature, our work is the first example that demonstrates cooperativity in a synthetic carbohydrate receptor.* These results could have diverse applications, ranging from cryptography to molecular computing, as well as providing fundamental insight into how carbohydrates are employed to convey information within cellular networks. Additionally, pioneering surface chemistry that enables us to control the size, orientation, and density of glycan patterns on various surfaces, with sub-micrometer

Note that all synthetic motors inevitably have some level of asperities, which must be incorporated in any useful model because a minor

dimensions, to mimic the presentation of glycans on cell surfaces has been established. Finally, a quantitative description for the motion of catalytic Au-Pt nanoswimmers that explain their diffusion and interaction with barriers has been developed.

#### D. Personnel Supported

Personnel	Percentage of Salary Provided by Grant
Stephen Rieth (Postdoc)	100%
Shudan Bian (Graduate Student)	unfunded
Matthew Miner (Graduate Student)	25%

#### E. Publications

1. Bian, S.; He, J.; Schesing, K. B.; Braunschweig, A. B.\* "Polymer Pen Lithography (PPL) Induced Site-Specific Click Chemistry for the Formation of Functional Glycan Arrays" *Small*, **2012**, 8, 2000–2005. DOI: 10.1002/smll.201102707.
2. Bian, S.; Schesing, K. B.; Braunschweig, A. B.\* "Matrix-assisted Polymer Pen Lithography induced Staudinger Ligation" *Chem. Commun.* **2012**, 48, 4995 – 4997. DOI: 10.1039/C2CC31615C.
3. Rieth, S.; Miner, M. R.; Chang, C. M.; Hurlocker, B.; Braunschweig, A.B.\* "Saccharide Receptor Achieves Concentration Dependent Mannoside Selectivity Through Two Distinct Cooperative Binding Pathways" *Chemical Science*, **2013**, 4, 357–367. DOI: 10.1039/C2SC20873C.
4. Takagi, D.; Braunschweig, A. B.; Zhang, J.; Shelley, M. J. "Dispersion of Self-Propelled Rods Undergoing Fluctuation-Driven Flips" *Physics Review Letters*, **2013**, 110, 038301. DOI: 10.1103/PhysRevLett.110.038301.
5. Zhong, X.; Bailey, N. A.; Schesing, K. B.; Bian, S.; Campos, L. M.;\* Braunschweig, A. B.\* "Materials for the Preparation of Polymer Pen Lithography Tip Arrays and a Comparison of their Printing Properties" *Journal of Polymer Science A: Polymer Chemistry*, **2013**, 51, 1533 –1539. DOI: 10.1002/pola.26513. Journal Cover.

#### F. Presentations

1. **Departmental Seminar SUNY Stony Brook, February 8, 2013**  
Carbohydrate Nanotechnology and Self-Assembling Complexity: Beyond Binary Solutions to Molecular Logic
2. **AFOSR Natural Material and Systems & Extremophiles Program Review, Washington D.C.**  
"Carbohydrate Nanotechnology: Hierarchical Assemblies and Information Processing with Oligosaccharide Host-Guest Systems"
3. **244<sup>th</sup> American Chemical Society National Meeting, Philadelphia, PA**  
"Using Polymer Pen Lithography to create new covalent bonds on surfaces with submicrometer feature diameters"
4. **244<sup>th</sup> American Chemical Society National Meeting, Philadelphia, PA**

- "Synthetic carbohydrate receptors achieve specificity through positive allosteric cooperativity"
5. **244th American Chemical Society National Meeting, Philadelphia, PA**  
"Matrix-assisted Polymer Pen Lithography: A new method for immobilization of bioorthogonal reactions and kinetic characterization of force catalyzed reactions"
  6. **University of Miami, Department of Chemistry, February 21, 2012**  
"A Mannose-Selective Synthetic Receptor With a Unique Cooperative Binding Mechanism"
  7. **AFOSR Natural Material and Systems & Extremophiles Program Review, Washington D.C., December 5, 2011**  
"Carbohydrate Nanotechnology: Hierarchical Assemblies and Information Processing with Oligosaccharide Host-Guest Systems"
  8. **Army Research Office, Durham, North Carolina, October 21, 2011**  
"Frontiers of Supramolecular Design: From Polymer Superstructures to Synthetic Lectins"
  9. **The Polytechnic Institute of New York University, October 7, 2011**  
"Decoding the Glycome with a New Family of Synthetic Lectins"
  10. **City University of New York, Staten Island, April 28, 2011**  
"Molecular Printing: Solving the sub-100 nm Soft Matter Conundrum"

#### **G. Consultative/Advisory Functions**

Reviewer: *Nature Nanotechnology*, *Nature Chemistry*, *ACS Nano*, *Macromolecules*, *Applied Physics A: Materials Science & Processing*, *Journal of Applied Polymer Science*, *Beilstein Journal of Organic Chemistry*, *RSC Advances*, *Air Force Office of Scientific Research (2011-2012)*, *Journal of Nanobiotechnology*, *Journal of Organic Chemistry*, *Small*, *Elsevier-Academic Press*, *Chemical Communications*, *Chemical Science*, *NSF Bio Division Review Panel (2012)*.

Session Chair, PMSE Young Investigator's Symposium, 244<sup>th</sup> ACS National Meeting

National Science Foundation BIO Review Panel

Applied Minerals, LLC Consulting

#### **H. New Invention Disclosures and Patents**

1. **Braunschweig, A. B.**; He, Jiajun; Bian, S.; Schesing, K. B. "Nanoreactor Printing" Non-Provisional Patent Application PCT/US12/32019
2. **Braunschweig, A. B.**; Rieth, S.; Miner, M. R. "Carbohydrate Selective Receptors" Provisional Patent Application[9]      **Braunschweig, A. B.**; Rieth, S.; Miner, M. R.
3. **Braunschweig, A. B.**; Bian, S. "Covalently Patterned Graphene by a Force Accelerated Cycloaddition Reaction" PCT/US13/44570

#### **I. Honors/Awards**

American Chemical Society Polymeric Materials: Science and Engineering (PMSE) Young Investigator Award (2014)

**Net Free Balance Report – Project F6928**

**PI/PD: Braunschweig, Adam**

AFOSR – “Carbohydrate Nanotechnology: Hierarchical Assemblies and Information Processing

From Oligosaccharide Synthetic Lectin Host Guest Systems”

4/15/2012 – 3/1/2013

<b>Account</b>	<b>Category</b>	<b>Approved Budget Y1 &amp; Y2</b>	<b>Expensed or Encumbered</b>	<b>Balance</b>
51103-51170	<b>Personnel</b>	<b>\$107,987</b>	<b>\$66,155.49</b>	<b>\$21,121.12</b>
63210	Apparatus Maintenance Laboratory Supplies Publications & Subscriptions Recruitment Telephones Equipment Rental Laundry & Linen Supplies Software	\$43,701	\$40,269.04	
	<b>Expendable Items</b>	<b>\$43,701</b>	<b>\$34,602.37</b>	<b>\$3,431.59</b>
	<b>Domestic Travel</b>	<b>\$2,040.00</b>	<b>\$1,638.20</b>	<b>\$401.80</b>
	Alnet Access Equipment Under \$500 Equipment Over \$500			
	<b>Non-Expendable Items</b>	-	-	-
60200	<b>Subcontract &lt; \$25,000</b>	-	-	-
60210	<b>Subcontract &gt; \$25,000</b>	-	-	-
76450	<b>Overhead on Subaward</b>	-	-	-
51173	<b>Tuition Remission</b>	-	-	-
65101	Publication Costs Univ. Repairs & Maintenance Duplicating Postage Research Service Facilities <b>Services</b>	\$2,000.00	-	
		<b>\$2,000.00</b>	-	<b>\$2,000.00</b>
	<b>TOTAL DIRECT COSTS</b>	<b>\$155,728.00</b>	<b>\$128,773.50</b>	<b>\$26,954.50</b>
	Carryover from Prior Year	-	-	-
	<b>NO INDIRECT COSTS</b>	-	-	-
	<b>INDIRECT COST BASE</b>	<b>\$155,728.00</b>	<b>\$128,773.50</b>	<b>\$26,954.50</b>
	<b>INDIRECT COSTS</b>	<b>\$84,094.00</b>	<b>\$67,872.85</b>	<b>\$16,221.15</b>
	Prior Month's Cumulative Expenses		-	
	<b>TOTAL COSTS</b>	<b>\$239,822.00</b>	<b>\$196,646.34</b>	<b>\$42,315.62</b>

# AFOSR Deliverables Submission Survey

Response ID:2722 Data

1.

## 1. Report Type

Final Report

## Primary Contact E-mail

Contact email if there is a problem with the report.

a.braunschweig@miami.edu

## Primary Contact Phone Number

Contact phone number if there is a problem with the report

3052842516

## Organization / Institution name

New York University / University of Miami

## Grant/Contract Title

The full title of the funded effort.

Carbohydrate Nanotechnology: Hierarchical Assemblies and Information Processing with Oligosaccharide-Synthetic Lectin Host-Guest Systems

## Grant/Contract Number

AFOSR assigned control number. It must begin with "FA9550" or "F49620" or "FA2386".

FA9550-11-1-0032

## Principal Investigator Name

The full name of the principal investigator on the grant or contract.

Adam B. Braunschweig

## Program Manager

The AFOSR Program Manager currently assigned to the award

Hugh DeLong

## Reporting Period Start Date

04/01/2011

## Reporting Period End Date

02/28/2013

## Abstract

Carbohydrates are used throughout nature to direct information processing and hierarchical assembly, but are rarely explored in the context of synthetic nanotechnology. Carbohydrates were explored as targets for synthetic receptors, in nanopatterning, and for directing the movement of nanoswimmers. A synthetic carbohydrate receptor that achieves the highest reported selectivity for mannosides over other pyranosides (28:1) via a unique cooperative binding mechanism has been developed. At high temperatures, a 2:1 receptor : mannose complex forms, and at low temperatures, a 1:2 receptor : mannose complex forms. The structures and thermodynamic binding properties of these complexes have been characterized by nuclear magnetic resonance

spectroscopy and molecular modeling. Additionally, Polymer Pen Lithography has been combined with the copper catalyzed azide-alkyne click reaction and the Staudinger Ligation, two bioorthogonal organic reactions, to create functional carbohydrate arrays. This patterning approach controls the position, orientation, and feature diameter of the deposited molecules to create sub-1 micrometer features of carbohydrates across centimeter-scale areas. Finally, a new mathematical model that describes the flipping, turning, and dispersion of gold-platinum catalytic nanomotors has been derived that explains their diffusion over long times and accounts for the imperfections on the nanorod structures that inevitably arise during any manufacturing process.

#### Distribution Statement

This is block 12 on the SF298 form.

Distribution A - Approved for Public Release

#### Explanation for Distribution Statement

If this is not approved for public release, please provide a short explanation. E.g., contains proprietary information.

#### SF298 Form

Please attach your [SF298 form](#). A blank SF298 can be found [here](#). Please do not spend extra effort to password protect or secure the PDF, we want to read your SF298. The maximum file size for SF298's is 50MB.

[form298\\_ab\\_d2.pdf](#)

#### Upload the Report Document. The maximum file size for the Report Document is 50MB.

[Braunschweig\\_Final\\_Report\\_AFOSR\\_YIP\\_2013\\_8\\_3\\_13.pdf](#)

#### Upload a Report Document, if any. The maximum file size for the Report Document is 50MB.

#### Archival Publications (published) during reporting period:

1. Bian, S.; He, J.; Schesing, K. B.; Braunschweig, A. B.\* "Polymer Pen Lithography (PPL) Induced Site-Specific Click Chemistry for the Formation of Functional Glycan Arrays" *Small*, 2012, 8, 2000–2005. DOI: 10.1002/smll.201102707.
2. Bian, S.; Schesing, K. B.; Braunschweig, A. B.\* "Matrix-assisted Polymer Pen Lithography induced Staudinger Ligation" *Chem. Commun.* 2012, 48, 4995 – 4997. DOI: 10.1039/C2CC31615C.
3. Rieth, S.; Miner, M. R.; Chang, C. M.; Hurlocker, B.; Braunschweig, A.B.\* "Saccharide Receptor Achieves Concentration Dependent Mannoside Selectivity Through Two Distinct Cooperative Binding Pathways" *Chemical Science*, 2013, 4, 357–367. DOI: 10.1039/C2SC20873C.
4. Takagi, D.; Braunschweig, A. B.; Zhang, J.; Shelley, M. J. "Dispersion of Self-Propelled Rods Undergoing Fluctuation-Driven Flips" *Physics Review Letters*, 2013, 110, 038301. DOI: 10.1103/PhysRevLett.110.038301.
5. Zhong, X.; Bailey, N. A.; Schesing, K. B.; Bian, S.; Campos, L. M.; Braunschweig, A. B.\* "Materials for the Preparation of Polymer Pen Lithography Tip Arrays and a Comparison of their Printing Properties" *Journal of Polymer Science A: Polymer Chemistry*, 2013, 51, 1533 –1539. DOI: 10.1002/pola.26513. Journal Cover.

#### Changes in research objectives (if any):

none

#### Change in AFOSR Program Manager, if any:

none

#### Extensions granted or milestones slipped, if any:

none

## 2. Thank You

---

### E-mail user

Aug 05, 2013 11:00:12 Success: Email Sent to: a.braunschweig@miami.edu

### Response Location

<b>Country:</b>	United States
<b>Region:</b>	FL
<b>City:</b>	Coral Gables
<b>Postal Code:</b>	33146
<b>Long &amp; Lat:</b>	Lat: 25.719999, Long:-80.270699